Measuring nearshore waves at break point in 4D with Stereo-GoPro photogrammetry: A field comparison with multi-beam LiDAR and pressure sensors

Marion Jaud, Stéphane Bertin, Emmanuel Augereau, France Floc'h

ISPRS Open Journal of Photogrammetry and Remote Sensing 14 (2024) 100077

Contents lists available at ScienceDirect

ISPRS Open Journal of Photogrammetry and Remote Sensing

journal homepage: www.journals.elsevier.com/isprs-open-journal-of-photogrammetry-and-remote-sensing

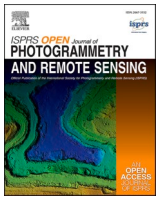

Measuring nearshore waves at break point in 4D with Stereo-GoPro photogrammetry: A field comparison with multi-beam LiDAR and pressure sensors

Marion Jaud [a,b,*], Stéphane Bertin [a], Emmanuel Augereau [a,b], France Floc'h [a]

[a] Geo-Ocean, Univ Brest, CNRS, Ifremer, UMR6538, F-29280, Plouzané, France
[b] Pôle Image et Instrumentation - IUEM, Univ Brest, CNRS, IRD, UAR 3113, F-29280, Plouzané, France

ARTICLE INFO

Keywords:
In situ wave measurement
Stereo-video
Sea state in surf zone
Optical calibration
Digital elevation model
Remote sensing

ABSTRACT

Measuring nearshore waves remains technically challenging despite wave properties are being used in a variety of applications. With the promise of high-resolution and remotely-sensed measurements of water surfaces in four dimensions (spatially and temporally), stereo-photogrammetry applied to video imagery has grown as a viable solution over the last ten years. However, past deployments have essentially used costly cameras and optics, requiring fixed deployment platforms and hindering the applicability of the method in the field.

Focusing on close-range measurements of nearshore waves at break point, this paper presents a detailed evaluation of a field-oriented and cost-effective stereo-video system composed of two *GoPro^{TM} (Hero 7)* cameras capable of collecting 12-megapixel imagery at 24 frames per second. The so-called 'Stereo-GoPro' system was deployed in the surf zone during energetic conditions at a macrotidal field site using a custom-assembled mobile tower. Deployed concurrently with stereo-video, a 16-beam LiDAR (Light Detection and Ranging) and two pressure sensors provided independent data to assess stereo-GoPro performance. All three methods were compared with respect to the evolution of the free-surface elevation over 25 min of recording at high tide and the wave parameters derived from spectral analysis. We show that stereo-GoPro allows producing digital elevation models (DEMs) of the water surface over large areas (250 m^2) at high spatial resolution (0.2 m grid size), which was unsurpassed by the LiDAR. From instrument inter-comparisons at the location of the pressure transducers, free-surface elevation root-mean square errors of 0.11 m and 0.18 m were obtained respectively for LiDAR and stereo-GoPro. This translated into a maximum relative error of 3.9% and 12.5% on spectral wave parameters for LiDAR and stereo-GoPro, respectively. Optical distortion in imagery, which could not be completely corrected with calibration, was the main source of error. Whilst stereo-video processing workflow remains complex, cost-effective stereo-photogrammetry already opens new opportunities for deriving wave parameters in coastal regions, as well as for various other practical applications. Further tests should try to address specifically challenges associated to variable ambient conditions and acquisition configurations, affecting measurement performance, to guarantee a larger uptake of the technique.

1. Introduction

Sea-state has an impact on a variety of issues related to coastal geomorphology (e.g., erosion, sediment transport) (e.g., Cowley and Harris, 2023; Nicholls et al., 2013), benthic habitats (e.g., stress on seagrass and coral beds) (e.g., Bulleri et al., 2018; Rattray et al., 2015), and renewable energy applications (e.g., Chella et al., 2012). Particularly, in coastal environments, the wave shape changes quickly approaching the coastline, making more complex the precise measurement of the time-resolved position of the free surface. However, coastal morphodynamics depends on the sediment transport induced by hydrodynamic processes directly generated by the wave shape and its spatio-temporal variability (e.g., Camenen and Larroudé, 2003; Grasso et al., 2011). Besides, wave impact forces on anthropogenic and natural structures such as harbor walls, wind turbine towers and cliffs are directly linked to the three-dimensional shape of the sea surface (Chella

* Corresponding author. IUEM, rue Dumont d'Urville, Technopôle Brest-Iroise, F-29280, Plouzané, France.
E-mail addresses: marion.jaud@univ-brest.fr (M. Jaud), stephane.bertin@univ-brest.fr (S. Bertin), emmanuel.augereau@univ-brest.fr (E. Augereau), france.floch@univ-brest.fr (F. Floc'h).

https://doi.org/10.1016/j.ophoto.2024.100077
Received 22 May 2024; Received in revised form 23 October 2024; Accepted 4 November 2024
Available online 6 November 2024

et al., 2012). Because sea state results from the combination of a large number of processes (oceanic waves being submitted to transformation along their propagation due to the presence of obstacles, variable bathymetry, wind stress and non-linear processes), observations are necessary to fully understand the role of these different processes.

Until recently, typical systems for directional wave measurements relied on time series retrieved from arrays of pressure sensors, acoustic wave sensors or wave gauge buoys (e.g., O'Reilly et al., 1996). These measurements, continuous in time, are point-wise and are less accurate if the waves are non-linear, with research indicating wave height under-estimation of 10% or more depending on the reconstruction method (Bonneton and Lannes, 2017; Martins et al., 2020).

To study the propagation of a wave train, and therefore its spatio-temporal evolution, measuring devices must be in capacity to provide space-time data with sufficient spatial coverage, spatial resolution and sampling frequency to capture irregularities, asymmetries and local phenomena (e.g., flash rip currents, Castelle et al., 2016). Close to the break point, measuring wave shape evolution requires in-situ measurements with spatio-temporal resolutions of the order of magnitude of decimeters and 0.1 s (O'Dea et al., 2021). Monitoring natural waves in their physical environment is thus very challenging yet crucial if we aim to make new advances in physics-based hydro-sedimentary numerical models, as well as improved predictions of future shoreline position and wave impact on structures.

In recent years, methodological developments around these issues have aimed at bridging the gap between large-scale but instant-wise monitoring, and continuous but point-wise measurements. In particular, research is increasingly making use of optical remote-sensing techniques with no direct contact (and therefore no interference) with the water body. Active methods mainly include X-band radar (Haller and Lyzenga, 2003) and Light Detection and Ranging (LiDAR) sensors, which can be used in 3D scan (Harry et al., 2010; Park et al., 2011) or 2D profiler mode, either in the green (Belmont et al., 2007; Horwood et al., 2005) or near infrared band (e.g. Blenkinsopp et al., 2010; Brodie et al., 2015; Harry et al., 2018; Martins et al., 2016). Martins et al. (2016) reported that the time required to carry out a 3D scan is inadequate for monitoring the propagation of wave crests, and commercial near-infrared multi-beam 2D profilers are now more commonly used (e.g., Baker et al., 2023; Feddersen et al., 2023; Harry et al., 2018; Martins et al., 2017; O'Dea et al., 2021). They can provide accurate measurements (e.g., a coefficient of determination of 0.89 and standard deviation of 47 mm in comparison to pressure sensors in the surf zone, Harry et al., 2018) at high temporal resolution, allowing run-up measurements and detailed wave shape characterization at breaking. Furthermore, although they have been essentially deployed from robust and generally fixed platforms (e.g., piers, dykes), the miniaturization of LiDAR sensors and their mounting on drone platforms now allow measurements seaward of the surf zone (Feddersen et al., 2024; Fiedler et al., 2021). Despite being very effective, LiDAR profilers measure water elevations along transects and thus do not provide true surface coverage. Besides, they remain expensive (e.g., 8 k€ at the time of purchase for the VLP16 presented in this paper).

Video imaging is a passive optical method widely used to extract characteristics of nearshore waves (e.g., Colvin et al., 2020), with the Coastal Imaging Research Network (CIRN) being an international consortium specifically developing and implementing new coastal imaging methodologies (Bruder and Brodie, 2020; Palmsten and Brodie, 2022). However, these methods are mono-video, whereas stereo-video surveys (i.e., stereo-photogrammetric methods using two cameras, the video acquisition adding the temporal component) allow to observe the free surface in 4D (three space dimensions + time). The principle of the method used to process pairs of images extracted from videos into a Digital Elevation Model (DEM) is described in De Vries et al. (2011). A processing software, WASS (Wave Acquisition Stereo System), has been specially developed for wave measurements by stereo-camera whose initial applications were the open sea (Bergamasco et al., 2017a). Most of the work carried out on stereo-video (Benetazzo et al., 2012; Leckler et al., 2015; Guimarães et al., 2020) used industrial cameras with low distortion lenses. Such cameras are relatively expensive (e.g., about 4 k€ for a BM-500GE JAI camera as used in Leckler et al. (2015) or Guimarães et al. (2020)) and fragile, while in-situ deployments pose the risk of instrument degradation or even loss due to adverse environmental conditions met in the field. These systems were therefore installed on robust structures, such as offshore platforms or harbor infrastructures (e.g., Bergamasco et al., 2017; De Vries et al., 2011; Guimarães et al., 2020; Leckler et al., 2015).

To limit the impact of eventual deterioration, and to be in capacity to multiply the number of measuring devices, low-cost strategies have been presented as promising alternatives, which are being deployed more lightly and more flexibly. Recently, Vieira et al. (2020) demonstrated the feasibility of free-surface reconstruction from the shore using a consumer-grade stereo system consisting of two smartphones. In their study, the validation of the system was only point-wise using a moored pressure sensor. Comparing their stereo-video system with the pressure sensor yielded Root Mean Square Errors (RMSE) of 0.1–0.12 m. Recent research also started investigating the possibility of using action cameras (Vieira and Soares, 2024) as robust yet low-cost alternatives to industrial cameras for field deployments. And, as with LiDAR, mounting the device on a drone offers a greater variety of viewpoints (Sawada et al., 2024). However, assessing measurement performance was generally limited to using a single pressure sensor, impeding spatial validation of stereo-video results, so that to date a meaningful comparison with LiDAR was solely attempted in the laboratory (Baker et al., 2023).

Despite sharing common issues, needs and research questions, practical implementations in the field and the laboratory differ significantly. In the laboratory, controlled conditions (e.g., lighting, bathymetry, water level, regular waves) facilitate obtaining good-quality data (e.g., imagery used in photogrammetry), and there is generally no need for data georeferencing. This simplifies the experimental protocol, limiting the multiplication of instruments (e.g., Global Navigation Satellite System - GNSS) and hence the propagation of errors in the final data. Besides, laboratories provide the advantage of simplified instrument installation and data quality evaluation. Yet, the lack of texture on the water surface and water transparency can represent difficulties for indoor experiments, for instance degrading tie point detection (Baker et al., 2023).

In this study, we compare a low-cost stereo-video device (using a pair of GoPro cameras) and a VLP-16 multi-beam LiDAR profiler for close-range measurements of nearshore waves at break point. These two spatialized acquisitions are also compared point-wise with a pressure sensor. Remote-sensing methods were deployed in the surf zone using a mobile tower at a macrotidal site during challenging conditions due to wave and wind. Stereo-GoPro and LiDAR measurements of the temporal evolution of the free surface elevation (water level) and spectral wave parameters were assessed over 25 min at high tide. The study is part of a larger project (ANR project WEST, "natural breaking WavEs and Sediment Transport during beach recovery") whose objectives are to evaluate the interactions between surface waves, hydrodynamics and bed slope leading to onshore net sediment transport in the surf zone during accretive conditions. Future work will employ stereo-video and LiDAR in conjunction with current and sediment concentration profilers providing colocalized measurements of the various parameters of interest.

The paper is structured as follows. After a presentation of the field site and experimental conditions in section 2, we detail the experimental setup (section 3) necessary to conduct the test, including the platform for instrument installation, the stereo-video system, as well as the pressure sensors and LiDAR deployed concurrently. Sections 4 and 5 present the purpose-built processing workflow adopted for reconstructing the water surface in 4D using the stereo-GoPro system and the methods used for inter-comparing the data with concurrent measuring devices. In the results section (section 6), the ability of the stereo-GoPro

to satisfactorily capture the temporal evolution of the free-surface in 4D is critically assessed, with at-a-point and spatialized comparisons with pressure sensor and LiDAR datasets. In section 7, we finally discuss the technical issues encountered, the potential of stereo-GoPro as a monitoring system for aquatic environments, as well as the limitations of this approach compared to other techniques (e.g., risk of distortion, dependence on ambient conditions, etc.) and avenues for further research, before concluding the study.

2. Field site and conditions

The field experiment we present in detail herewith took place on November 22, 2022 at Porsmilin, a sandy beach with a long-term coastal monitoring program (Bertin et al., 2022a, 2022b) situated in Brittany (northwest France) (Fig. 1a). Several tests performed beforehand with an increasing level of complexity (e.g., indoor camera calibration, measurement of fixed and scaled topography such as buildings, field deployments using harbor walls as a sturdy platform for installing cameras) served to design and optimize the experimental setup (section 3.1) and processing workflow (section 4) used in this study. The latter was elaborated to allow for a realistic field evaluation through a comparison with two independent techniques, namely pressure sensors and LiDAR.

To enable direct comparisons between measuring devices, a common coordinate system was used. Geographic coordinates were referenced to the French legal systems for this region, i.e., RGF93-Lambert 93 for planimetry and NGF-IGN69 for altimetry (elevation zero corresponding to approximately 0.5 m below mean sea level).

With a simple access, in particular the presence of a carpark fronting the beach and a boat ramp, making for practical on-site camera calibration and setup installation and removal, Porsmilin beach represented a convenient field site for the experiment. The beach is approximately 200 m wide in the longshore direction and is moderately indented. Inland and to the north, the beach is separated from a brackish water marsh by a small dune cordon (about 1–2 m tall). To the east and west, it is flanked by cliffs of about 15 m in height and bounded by rocky reefs extending offshore. The median sediment grain size (D50) is 320 μm (Dehouck et al., 2009). The beach responds quickly to changes in wave conditions, with beach slope in particular found to vary both spatially and temporally. The modal morphodynamic beach state and type is intermediate low-tide-terrace, with the upper beach eventually reaching a reflective state particularly over summer months, with the formation of a berm. A cross-shore transect was measured using GNSS and Real Time Kinematic positioning (RTK-GNSS) the day of the experiment (Fig. 1b), indicating a slope of 5.5% over the upper beach, where our experimental setup was installed.

The experiment took place during an energetic swell event characterized by relatively large waves and a moderate to fresh cross-onshore breeze (force 4–5 on Beaufort wind scale), providing challenging conditions representative of what can be considered a moderate storm at

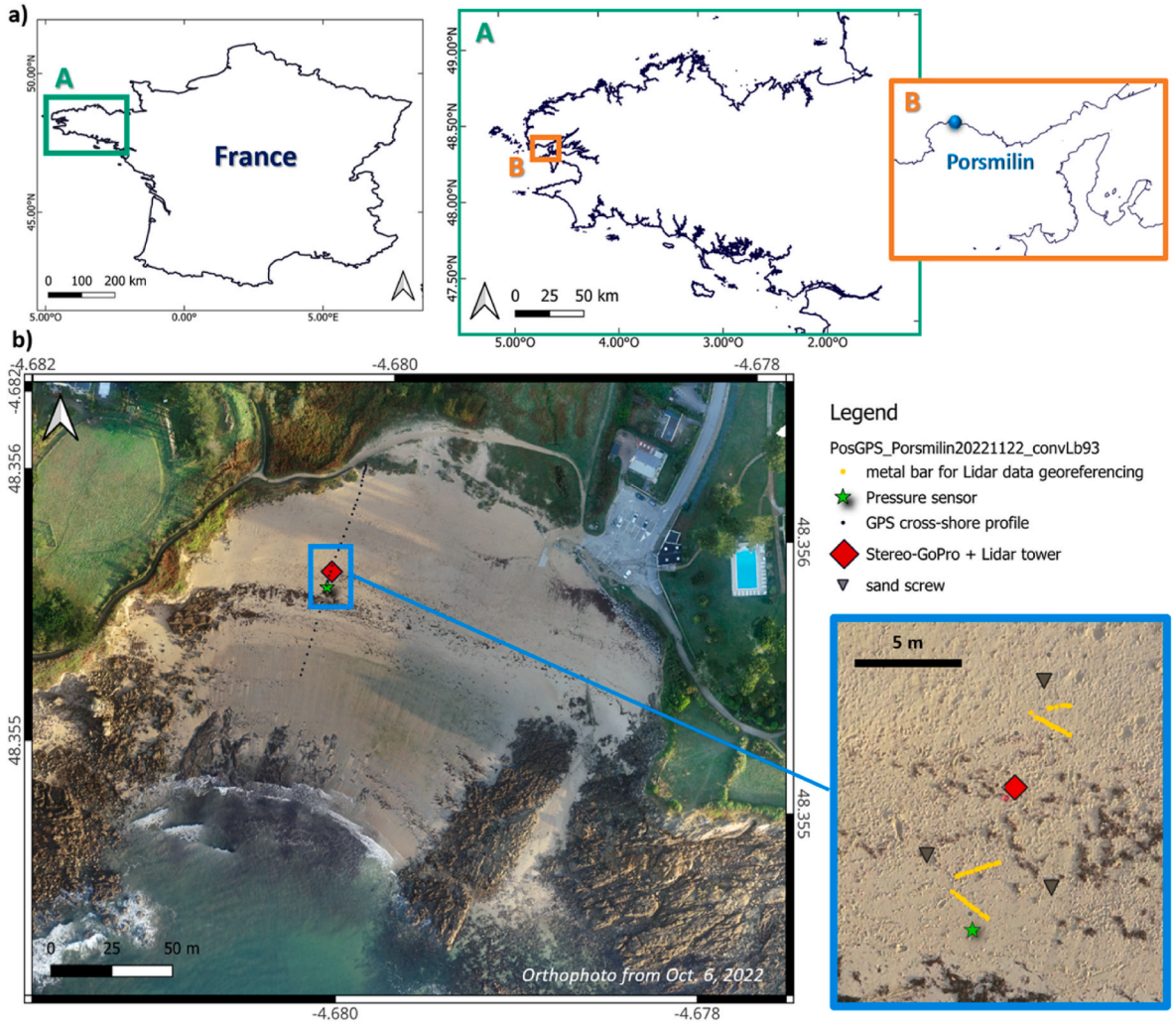

Fig. 1. a) Location of the experimental field site at Porsmilin beach in Brittany (northwest France). b) Aerial orthophoto of Porsmilin beach at low tide showing the position of the equipment deployed for the test.

Porsmilin. Wave forecast called for a long-period (14 s) swell, fading during the day, with an offshore wave direction from the WNW and a breaking wave height between 1.2 and 2 m (offshore wave height in excess of 4.5 m at Pierres Noires buoy in 60 m depth). Tides, semi-diurnal, fall in the macrotidal range (mean tidal range is 5.7 m during spring tides). High Tide (HT) was at 15:36 (UTC+1), with a predicted tidal range of 4.8 m. Surge (i.e., the excess water level not due to astronomical tides) was predicted to be below 0.1 m during the survey, which was verified using observations at the nearest gauge station of Le Conquet (8 km distant from Porsmilin). The wind was from the W-WNW (average speed of 11–16 knots) with gusts in excess of 20 knots, according to forecast.

In terms of illumination and sun angle, important for field photogrammetry and certainly even more when it comes to measuring a water surface, the survey being in Autumn meant the sun was low and due to the orientation of the beach (~195° or SSW), it would eventually face the cameras if looking in a cross-shore direction. The sun position in terms of zenith and azimuth was 14° and 215°, respectively, at the time of high tide. However, throughout the test, the sky was mostly overcast, which limited the occurrence of sunglint at the water surface, and considering the results obtained made for favorable lighting conditions.

3. Material and experimental setup

During the experiment, we deployed in parallel three independent wave measuring devices, and efforts were made to obtain comparable results. Instruments were installed and prepared at low tide (e.g., calibration, georeferencing), while water surface measurements were carried out at high tide when waves were the largest.

Our preliminary tests showed that stereo-video and LiDAR were both limited distance-wise (cf. sections 3.1 and 3.3), which prompted for a deployment as close to the waves as possible. Porsmilin not disposing of a pier or similar type structures traversing the beach, which have been used in past studies for installing LiDAR or video cameras (e.g., Ojeda and Guillén, 2008; Phillips et al., 2019), we had recourse to a sturdy metal tower made of several blocks, requiring ~1.5h to be mounted in the field by three people. The tower was 5.5 m tall for a total weight of approximately 50 kg. The position of the tower on the beach (Fig. 1b) was chosen to find a compromise between closely observing the waves breaking and limiting the immersion of the tower during measurements. The tower was installed at an altitude of 2.7 m, equivalent to approximately 2.2 m above mean sea level, and implied a maximum (tidal) water level at the foot of the tower of 0.8 m at high tide. The tower was moored to the beach by a system of shrouds and sand screws so as to remain in place for the duration of a tidal cycle. Our observations suggest that the structure hardly moved despite wave attack and sustained wind, with no noticeable effects on measurements.

3.1. – Stereo-GoPro system

GoPro cameras offer several advantages specifically tailored for outdoor filming: they are designed to be durable, rugged and water resistant. Being also compact, lightweight and relatively inexpensive, they can be installed on any type of fixed or mobile platforms. With improved optics and functionality, they have become a very flexible imaging system including for scientific applications (e.g., Li et al., 2018; Nocerino et al., 2020; Torkan et al., 2022). To form the stereo system, we used two *GoPro™ Hero7* cameras in 4K video mode (4:3 format and a framerate of 24 images/s), with an image resolution of 12 Mega-pixels. The cameras have a very short focal length (f = 2.92 mm), resulting in a very wide field of view (94.4° and 122.6° along the vertical and horizontal for 4:3 format, respectively). A short focal length is however accompanied by optical distortion effects in GoPro images, which must be correctly estimated and corrected through calibration (section 4.1) before accurate 3D reconstructions.

During the experiment, cameras were operated remotely via WiFi. Their precise synchronization was ensured using a luminous flash as clapperboard, from which we determined the time shift (number of frames of difference) between the two videos. To avoid recording latency, and hence to limit any time drift within videos, cameras were equipped with "V30" high-speed micro-SD cards. This way, drift was measured to be less than 0.04 s (i.e., one frame difference) after 15 min of recording, which we found was approximately half that of conventional SD cards, and prevented the introduction of additional errors due to video de-synchronization.

Cameras were housed in specially adapted watertight enclosures mounted on a rigid stainless-steel tube, forming a relatively light-weight (~1 kg per camera block) and secure system (Fig. 2b). Cameras can be moved on the tube, and rigidly secured at a fixed position, hence allowing varying the baseline distance between the two optical centers to adapt to different situations. The stereo system was placed on a cradle for transport and fixed to a topographic tripod for the calibration stage (section 4.1). During the survey, it was mounted atop the metal tower, at a height of ~5.5 m, corresponding to a minimum height of 4.7 m above the (still) water surface at high tide.

The baseline-to-distance ratio, noted here B/D, is a characteristic parameter of the setup. A large B/D ratio improves the accuracy of 3D reconstruction and limits noise. On the other hand, if B/D becomes too large, images are acquired from too different angles and it becomes impossible to detect homologous points to be used in feature points matching. One difficulty in designing the setup is therefore to find an appropriate B/D ratio. Bergamasco et al. (2017) reported that the optical axes of the cameras should be quasi-parallel and that the B/D ratio should be kept low, about 0.1. In the Vieira et al. (2020) study, with a baseline of 0.98 m and an imaged window ranging from 10 m to 35 m, B/D varied from 0.1 to 0.03 (near to far).

In the present study, provided GoPro cameras have a short focal length and are better suited to close-range imagery, this added a constraint on the maximum value of D, and therefore on the choice of baseline B. In light of previous work, and informed by design simulations in MATLAB® mimicking our field configuration, a baseline of 1.1 m was selected for this field experiment. Cameras were installed with optical axes parallel and oriented at an angle of 40° to the vertical. This configuration resulted in a measurement area (at the overlap between the two images, where 3D can be reconstructed) of approximately 30 m (cross-shore) by 40 m (long-shore) with a trapezoidal shape, the closest measured point being at a horizontal distance of less than 1 m from the tower, and a B/D ratio ranging from 0.26 to 0.036 (near to far). Spatial resolution (i.e., ground sampling distance, GSD) varied as a function of the position on the image (oblique viewing) and time (variation in water level). Using photogrammetric equations under the assumption of a pinhole camera model, GSD was modeled to vary from as low as 3 mm/pixel up to 16 mm/pixel in the distal part, at the time of high tide.

3.2. – Pressure sensors

Two OSSI Wave Gauge pressure transducers (referred to as PT1 and PT2) were deployed at low tide to provide independent data to assess stereo-GoPro and LiDAR measurements. Sensors were mounted side-by-side using a sand screw, and positioned within the shared measurement area 6 m seaward of the tower (Fig. 2). Sensors were installed upside down to have the pressure measurement cell flush with the seabed. Sensors were synchronized to GNSS time (coordinated universal time) by immerging the sensors prior to the experiment and noting the time of immersion, and configured to continuously acquire data at the highest possible frequency of 5 Hz from the time the system was installed until it was dismantled.

During processing, pressure readings were corrected from i) atmospheric mean sea level pressure recorded three-hourly at the closest MeteoFrance station (Guipavas, ~20 km distance), which essentially sets the mean water level after correction, and ii) non-hydrostatic pressure following linear wave theory (Bishop and Donelan, 1987;

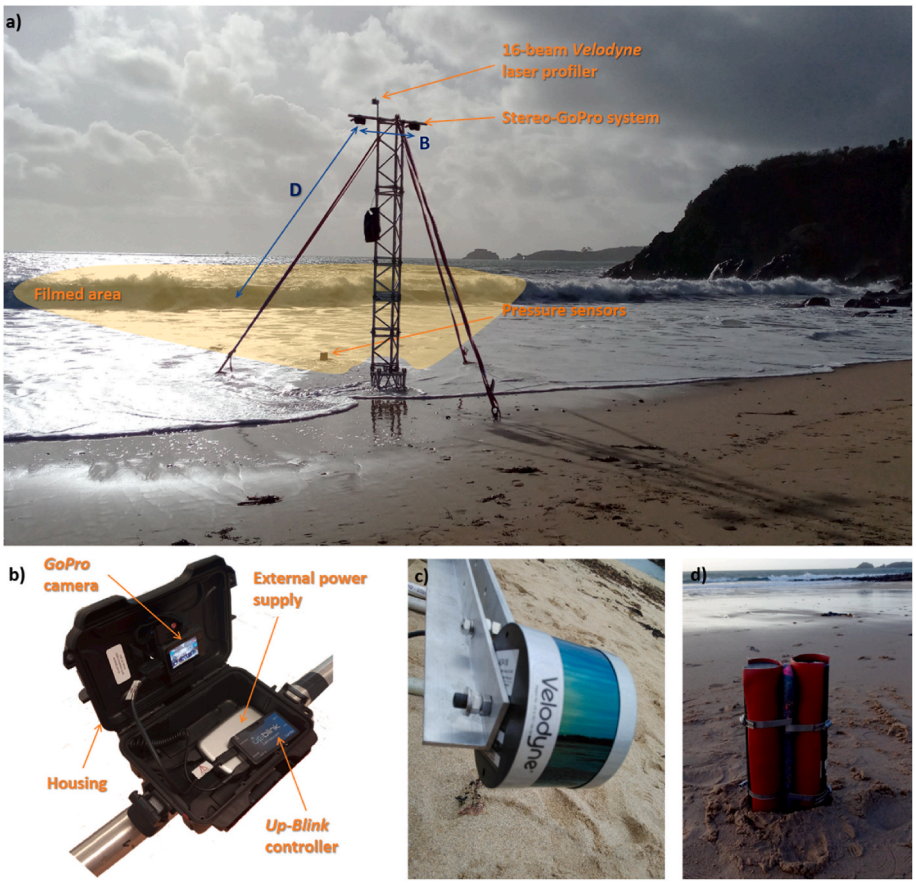

Fig. 2. a) Experimental setup showing the Stereo-GoPro system and the multi-beam laser profiler installed atop a 5.5 m tower, and the pressure sensors partly buried in sand within the shared measurement area. The photo was taken during the flowing tide. Close-up view on b) the camera system, c) the 16-beam Velodyne laser profiler, and d) the two pressure sensors attached to a sand screw.

Hom-ma et al., 1966). Pressure data were used to compute spectral wave parameters (e.g., Hm0, Tm02 and Tp) in gravity and infragravity bands (cf. section 5), and to reconstruct the free-surface elevation (i.e., water level). Free-surface elevation, initially expressed in terms of elevation above the sensor, was transformed to the reference vertical datum (NGF/IGN69) using GNSS coordinates of the sensor location obtained at low tide.

Using two sensors maximized the chance of collecting data (in the case of instrument failure), and through results' intercomparison, represented a simple way to assess the quality of data produced via pressure measurement and processing. Free-surface comparison over the testing period (25 min at high tide), with a mean water depth of 0.7 m, showed an average (signed) error of 0.07 m and a standard deviation of 0.05 m (Pearson's correlation coefficient $R = 0.98$, $p < 0.05$). Vertical bias between PT1 and PT2 was attributed to pressure variations when the sensors were exposed to ambient light and heat, which made for correcting the atmospheric pressure error prone. Measurement uncertainty on wave parameters amounted to just 1.2% on Hm0 (corresponding to a difference of ~0.01 m) and 1% on Tm02 (i.e., a difference of ~0.06 s). For comparison with stereo-video and LiDAR (section 5), PT1 was arbitrarily chosen as the reference.

3.3. – *Multi-beam laser Profiler*

Besides stereo-video and pressure sensors, a Velodyne VLP-16 Puck® (Fig. 2c) laser profiler (or LiDAR) was also deployed for the experiment, emitting 16 rotating laser beams in the near infrared (905 nm), and representing a direct method for measuring the water surface along the 16 profiles. The laser was fixed vertically to the top of the tower at a height of ~5.8 m above the seabed (i.e., slightly above the stereo system), corresponding to a minimum distance of 5 m above the water surface (Fig. 2a). Laser beams were aligned essentially cross-shore and the water surface both seaward and landward of the tower was measured due to a rotation at 360° during one revolution of the laser head.

The VLP-16 profiler was powered by an external battery (12 V - 17 Ah) and was set to a sampling frame rate of 10 Hz (10 revolutions per second). Data was recorded on a field computer connected via Ethernet with acquisition started by a programmable switch at a predefined time. Each laser impulse was time-tagged to the nearest micro-second, the timestamp corresponding to the time elapsed since the LiDAR was switched on.

According to manufacturer specifications, the VLP-16 has an angular resolution of 0.1° and 2° along the horizontal and vertical directions, respectively, a typical accuracy of ±0.03 m, and a maximum working range of 100 m. The latter was estimated on solid surfaces with a normal viewing angle, and is expected to be less when measuring a water surface obliquely, due to water absorption and reflection of LiDAR rays.

For georeferencing LiDAR measurements, four metal rods (2-m long and 0.1-m wide), whose positions were measured with centimeter accuracy using RTK-GNSS, were laid out non-parallel on the sand at low tide to create a variation in topography visible by the laser (Fig. 1b). This enabled calculating a projection matrix of the laser profiles. As the laser was kept fixed, it was assumed the projection matrix remained valid throughout the survey.

4. Method of stereo-video

4.1. Calibration

Not using metric (i.e., manufacturer calibrated) cameras, the ability to reconstruct the water surface from stereoscopic images relied on camera calibration. Calibration consists of calculating the intrinsic (e.g., focal length, principal point and distortion coefficients) and extrinsic (3D translation and rotation between cameras) that will bring the real images, impacted by lens distortion and projective geometry (due to oblique viewing), to a "pinhole" theoretical geometry.

For the sake of simplicity and performance, we opted for a pre-calibration of the setup using a 2D planar and stiff checkerboard (Fig. 3). To be used in the field at the working distances considered required a large checkerboard (0.7 m × 0.7 m with 0.05 m alternating black and white squares). Calibration images of the checkerboard were processed using the Stereo-Camera Calibrator toolbox in MATLAB®, which enables sub-pixel and automatic corner detection and provides simultaneously the intrinsic and extrinsic parameters of the camera pair.

In order to minimize calibration time and hence save battery power, a calibration procedure was implemented (Fig. 3a). It was designed to allow for a simple and efficient on-site application and to be easily replicable, to maximize the chance of obtaining consistent results with the method. The checkerboard was mounted on a tripod in order to limit its movements during image acquisition. The stereo system was moved to six different positions (left/central/right and near/far, shown by red crosses in Fig. 3a) relative to the checkerboard. For each position, the checkerboard was rotated along a vertical axis to obtain three different orientations. In addition, the stereo-video mounting bar was rotated around a horizontal axis so that the checkerboard covered the entire image vertically (bottom/center/top). Thus, nine imaging configurations were obtained for each position of the stereo setup (Fig. 3c). This led to a total of 54 pairs of images extracted for calibration. A few additional stereo pairs were collected for calibration verification. For this study, capture of calibration and verification images was realized at Porsmilin before installing the setup on the measurement tower, and took approximately 5 min.

For evaluating calibration quality, the Stereo Camera Calibrator toolbox provides a quality score for each calibration image through the reprojection error (i.e., distances, in pixel, between the detected and the reprojected checkerboard corners, Fig. 4a–b). To complete this quality estimation, we computed the rectification error (Bertin et al., 2015) on three verification stereo pairs. In epipolar geometry, homologous points between left and right images are situated on the same horizontal line. Hence, the rectification error corresponds to the vertical distance in pixel between two homologous points (i.e., checkerboard corners, Fig. 4c).

For the experiment presented, we obtained a reprojection error of 2.4 pixels on average, while the rectification error showed slightly improved statistics with a mean and a maximum error of 1.1 and 1.7 pixels, respectively. After calibration, we took great care to have as minimal disturbances of the stereo setup as possible, to ensure that calibration parameters, in particular camera baseline and rotations, remained unchanged throughout the test duration.

4.2. Wave stereo-reconstruction

Stereo-reconstruction was performed with MicMac (Rupnik et al., 2017: https://github.com/micmacIGN/micmac), an open-source photogrammetry software developed by the French National Geographic Institute (IGN) and adapted to a wide range of approaches (e.g., Structure-from-Motion and stereo-photogrammetry, with satellite, aerial and terrestrial vectors). Stereo-images of the water surface were processed using an automated and purpose-built workflow (Fig. 5) written in MATLAB® in which MicMac functions are called. In essence, the workflow allows reconstructing a georeferenced Digital Elevation Model (DEM) from stereo pairs of the water surface. A description of the complete workflow follows and is summarized in Fig. 5.

After camera synchronization (cf. section 3.1), one image every five (equivalent to a sampling rate of 4.8 Hz) is extracted from synchronized GoPro videos, images being renamed according to the date and time of acquisition. Following, stereo images are corrected from distortion using the Stereo Camera Calibrator toolbox, applying the intrinsic parameters obtained during calibration. The distortion-corrected images are then

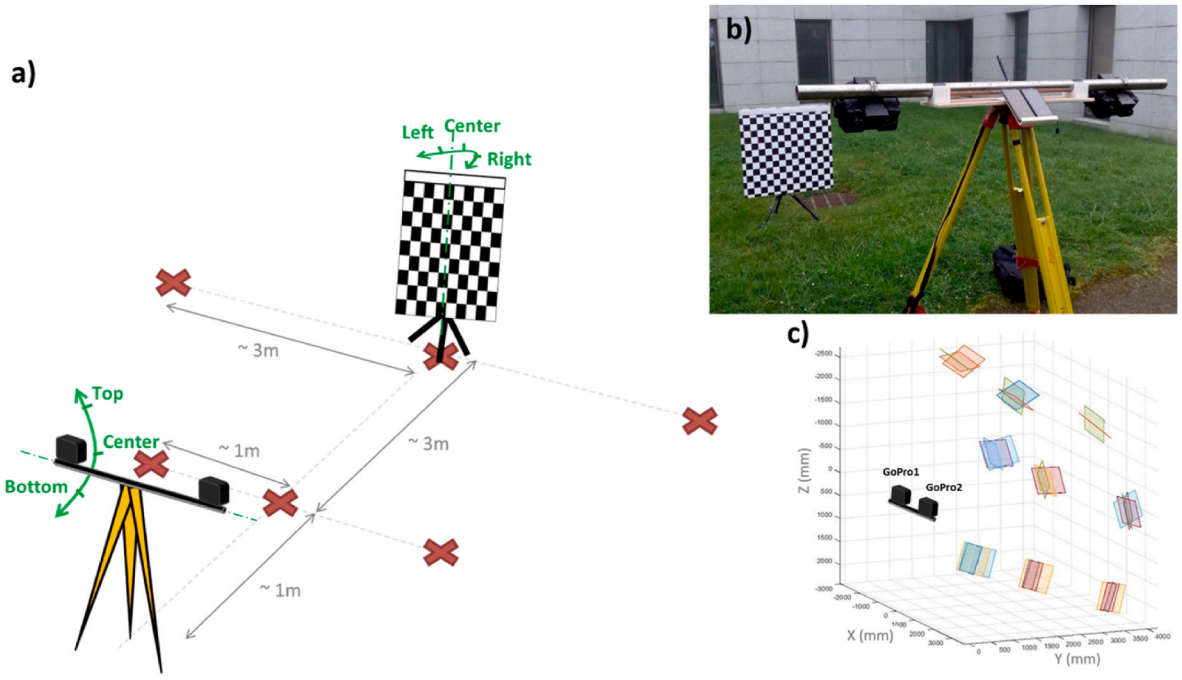

Fig. 3. a) Schematic of the procedure implemented to calibrate the stereo-GoPro system using a 2D checkerboard. b) System configuration for obtaining calibration and verification images, with the stereo-GoPro setup mounted on a topographic tripod. c) Spatial distribution of the checkerboard for 27 calibration images corresponding to the three distal positions in subset (a) (nine orientations each).

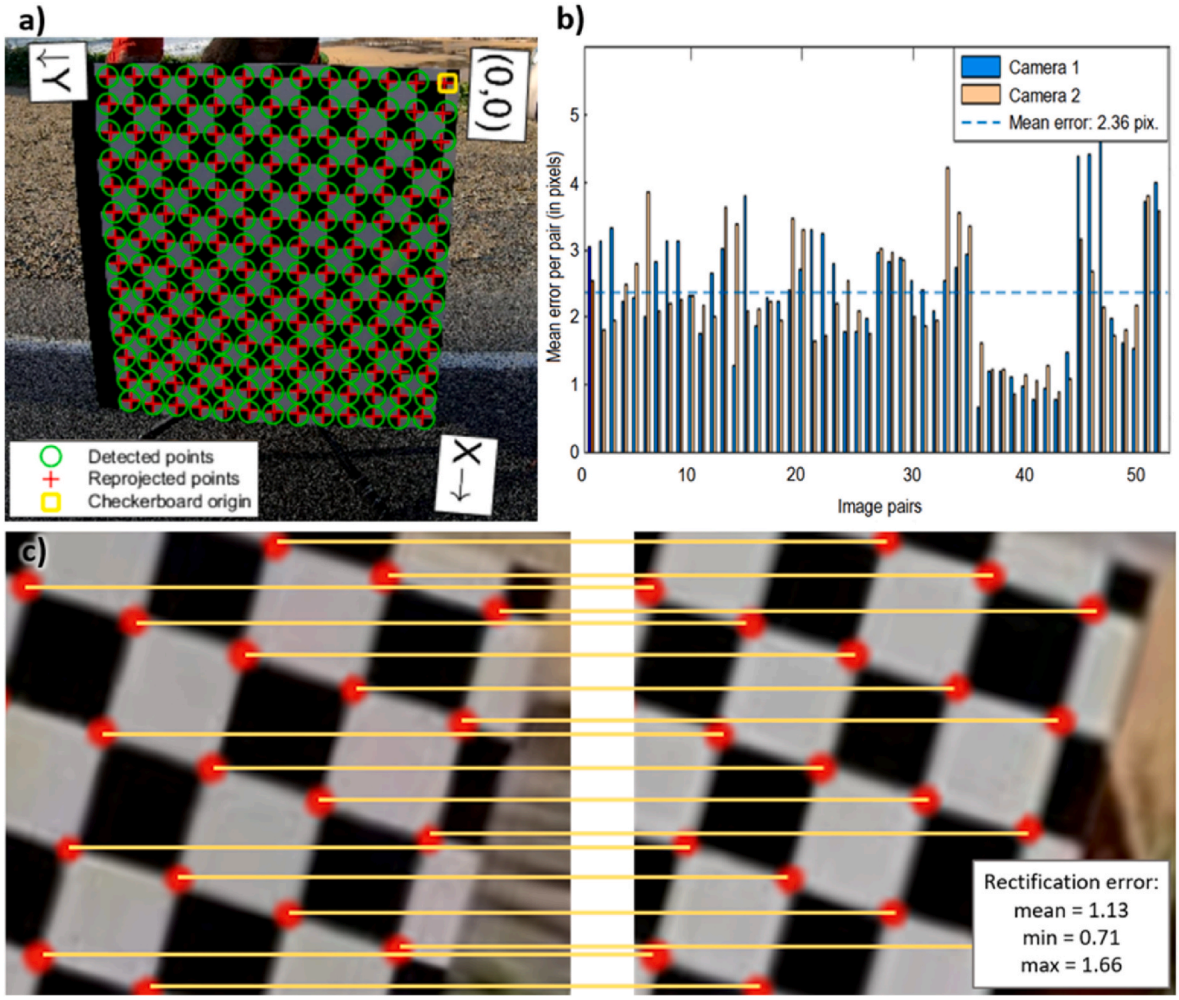

Fig. 4. Evaluation of calibration quality: (a) and (b) reprojection errors for each camera over all calibration images; (c) rectification errors, calculated a posteriori on three stereo pairs complementary to the calibration data set.

processed using MicMac functions, according to the following steps.

- The Autocal and Orientation files are updated respectively with the focal length of the cameras and the components of the baseline vector determined during calibration.
- The command "Tapioca" is launched for computing tie points on the full resolution images.
- The command “Tapas” allows computing purely relative camera orientations. By using the "Figee" option, the algorithm is forced to use the parameters calculated during calibration.
- The command “AperiCloud” generates a sparse 3D cloud.
- Finally, the command “C3DC” computes a dense point cloud. Among the available options, we obtained the best results with the "Forest" option (epipolar matching).

A georeferencing matrix was calculated from five Ground Control Points (GCPs) visible in the imaged area at low tide and measured independently using RTK-GNSS. This matrix was applied to all stereo-video point clouds, thereby assuming a fixed setup geometry over time.

3D point clouds typically covered trapezoidal areas, starting 1 m from the foot of the tower, with point density decreasing rapidly with distance from the cameras (from a maximum density in excess of 10,000 points/m^2 to just a few hundred points/m^2 in the far field). To limit the impact of too low spatial resolutions, the measurement area was systematically cropped according to a minimum density threshold. The density threshold was selected based on considerations regarding the optimal resolution of the water surface DEMs reconstructed using the workflow. In our case, the cropping mask corresponded to the area where the average density was superior or equal to 75 points/m^2. It was calculated over the first 50 point clouds since density calculation at each point is a numerically intensive task.

Besides, point cloud filtering was undertaken removing any points (outliers) with a deviation from the mean (calculated over a 1-m radius) greater than three times the standard deviation. This removed 5300 outliers on average (std = 615) per point cloud, corresponding to approximately 3.9% (sigma = 0.23%) of the initial number of points. Finally, point clouds were interpolated onto a regular 0.2 m grid to form a series of DEMs. DEM grid resolution (0.2 m) was adapted to the minimum point cloud density (75 points/m^2), using the recommendation to have at least three points for interpolating an elevation value at a given DEM grid node.

For the analysis that follows, extracted image frames originating from separate video files resulted in small gaps in stereo-video data (maximum gap ~15 s), a limitation that will be corrected in the future. The stereo-video dataset represented nearly 8450 images per camera (n = 8446) and required over 200 h of processing to transform raw images into final DEMs, the most time-consuming steps being point cloud densification (24%), and DEM generation, including point cloud filtering (72%).

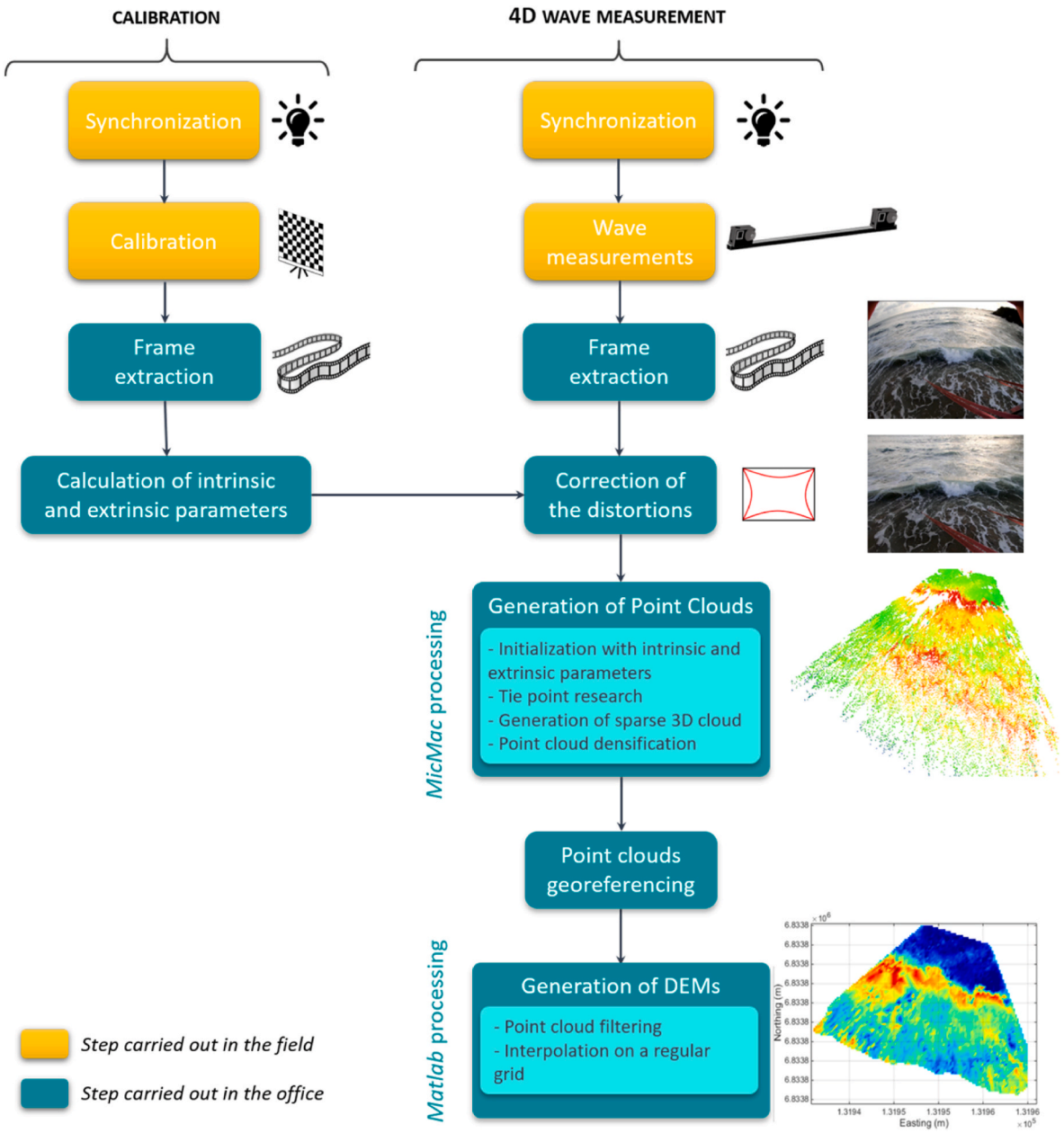

Fig. 5. Processing workflow for 4D reconstruction of the water surface from stereoscopic images.

5. Methods inter-comparison and error evaluation

All three methods were compared with respect to i) the evolution of the free-surface elevation and ii) wave parameters derived from spectral analysis over 25 min of recording, measurements taking place inside the surf zone. To enable direct and meaningful comparisons, free-surface elevations measured by the pressure sensor (initially at 5 Hz) and LiDAR (initially at 10 Hz) were resampled (linear interpolation) to the sampling frequency of stereo-video (4.8 Hz).

As a first step, the free-surface elevation measured by the pressure sensor was used as reference for assessing stereo-video and LiDAR quality. Quantitative error metrics such as the mean difference (or vertical bias), representing the vertical offset between water level time-series, and the standard deviation, representing measurement precision, were computed from the temporal comparisons.

Method comparison was also carried out in terms of spectral wave parameters calculated from the free-surface elevations. Time-series were first detrended to remove tidal influence, before Welch's power spectral density (PSD) was estimated using a block size of 512, a 50% overlap, a confidence level set at 95%, and a burst duration of 20 min, implying a single burst over the 25 min of comparison. The distribution of spectral density was used to determine the peak frequency in gravity band (we used 0.04 Hz and 0.5 Hz as bounding frequencies), which was used in turn to separately calculate wave parameters in gravity and infragravity bands, separation being done at half the peak frequency. Wave parameters reported here are the significant wave height (Hm0), the mean absolute wave period (Tm02), and the peak wave period (Tp).

To go beyond a temporal validation at a single point (the location of the pressure sensor), stereo-GoPro DEMs of the water surface were compared with LiDAR point clouds at corresponding times. Unlike stereo-video, LiDAR is an active technique and does not involve several processing steps (apart from georeferencing), which may imply a reduced error rate compared with the more complex stereo-video workflow. Comparisons were performed using cloud-to-mesh distance calculations in CloudCompare®, from which error statistics such as the mean error (ME) and the standard deviation of error (SDE) were

estimated. We recall that all measurement devices were synchronized to GNSS time (UTC) with water level expressed using a common vertical reference (NGF/IGN69), which facilitated comparisons.

6. Results

6.1. Water surface 4D reconstruction with stereo-GoPro

Fig. 6 shows the measurement coverage for the different systems deployed during the field experiment. For Stereo-GoPro, it corresponds to the measurement coverage after cropping, filtering and interpolating the initial point clouds, that is the final data analyzed hereafter. Stereo-GoPro DEMs cover approximately 250 m^2, corresponding to a cross-shore extent of 16 m and a lateral extent varying from 7.6 m to 25 m. Thanks to the wide field of view of GoPro cameras, lateral coverage is almost three times that of the Velodyne-16 laser profiler. The LiDAR survey covers a longer cross-shore window. Yet, the smaller the angle of incidence of the beams in relation to the water surface, the lower the cross-shore density. Consequently, LiDAR point density decreases rapidly with distance from the tower. On average, the cross-shore distance between consecutive LiDAR points is 0.02 m at 1 m from the tower and 0.27 m at 16 m from the tower. In comparison, stereo-GoPro produced an average initial point spacing of 0.11 m at a 16-m distance (75 points/m^2), from which DEMs with a regular spacing of 0.2 m were produced. In terms of LiDAR inter-beam distances, it is 0.17 m and 0.7 m at 1 m and 16 m from the tower, respectively, which means a lateral LiDAR resolution more than three times coarser than stereo-GoPro at a 16-m distance.

Fig. 7 shows a series of five consecutive observations (with a time-step of 0.4 s) of a breaking wave obtained using the stereo-GoPro system, at different stages of processing: raw images, images corrected of geometrical distortion, and the resulting DEMs. DEMs show variations of the water level surpassing 1 m, from trough to crest (shown in blue and red, respectively). Water level variations are not uniform alongshore, which could suggest the benefit of 4D compared to localized (e.g., pressure sensor) measurements for capturing the complexity of near-shore water surfaces. Visually, the DEMs depict the progression and breaking of a single wave in front of the measurement tower. At first, the wave inflates without breaking, followed by a lowering of the water surface at the wave toe shown by darker blue, together with a grouping of high elevations at the wave crest during plunging and collapse. Red shrouds, used for keeping the measurement tower steady, visible in the photographs were filtered automatically during processing and do not appear in DEMs, which would otherwise create abnormally high water surface elevations underneath. Although it is difficult to ascertain, Fig. 7 suggests that foam was correctly reproduced by measurements, due perhaps to lighting conditions and video acquisition resulting in the foam being well textured.

6.2. Assessment of stereo-GoPro data quality

Fig. 8 presents the evolution of the free surface measured independently by the pressure sensor and linear theory, LiDAR and stereo-GoPro system over 25 min at high tide. Unlike LiDAR and pressure sensor data, which are continuous, water level time-series produced by stereo-GoPro present two gaps (about ~15 s - see e.g., holes in data at 14:24 and 14:33). Qualitatively, Fig. 8 suggests a good agreement between measurements, evidenced by coinciding (in time) major peaks and troughs of the free surface for the three methods. However, distributions of the free-surface elevations show differences between measuring devices, such as the presence of a vertical offset (i.e., mean bias) between measurements, with pressure sensor data appearing below stereo-video and LiDAR (Fig. 8b). Besides this vertical offset, the shape of the distributions differs, with in particular pressure sensor data showing two peaks at 3 m and 3.2 m (i.e., around the mean water surface), while LiDAR data show three peaks and stereo-video only one peak. More detailed observations on the insert showing a 2-min recording (Fig. 8c) also suggest a higher level of noise in stereo-video data, shown by a multiplicity of secondary peaks and troughs which are not apparent in pressure sensor and LiDAR data. Differences between stereo-video (respectively, LiDAR) and pressure sensor (Fig. 8c–d) are generally contained within the range $\pm$ 0.5 m and are more frequent for stereo-video. Differences are exacerbated at wave crests and troughs. Overall, the free-surface elevation measured by LiDAR appears to be coherent with the pressure sensor, although generally presenting larger peaks (i.e., higher crest of the wave, see for instance the wave at 14:27:15 whereby LiDAR is above

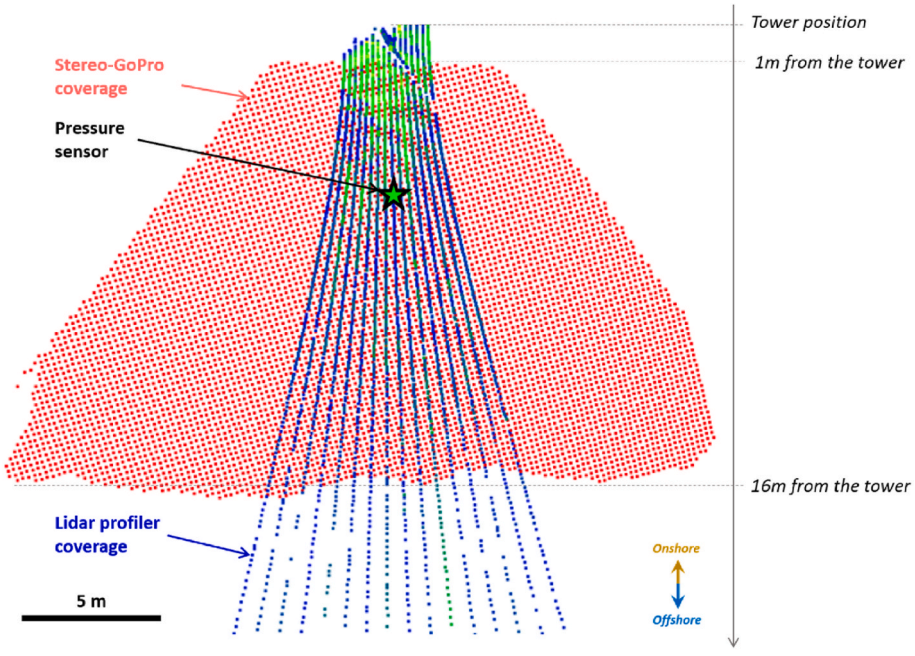

Fig. 6. Survey coverage for the instruments used during the study. Stereo-GoPro coverage corresponds to a typical DEM after cropping, filtering and interpolating the point cloud onto a 0.2 m grid. The color scale applied to the laser beams corresponds to the relative intensity of the laser return (blue: low intensity/green: high intensity). (For interpretation of the references to color in this figure legend, the reader is referred to the Web version of this article.)

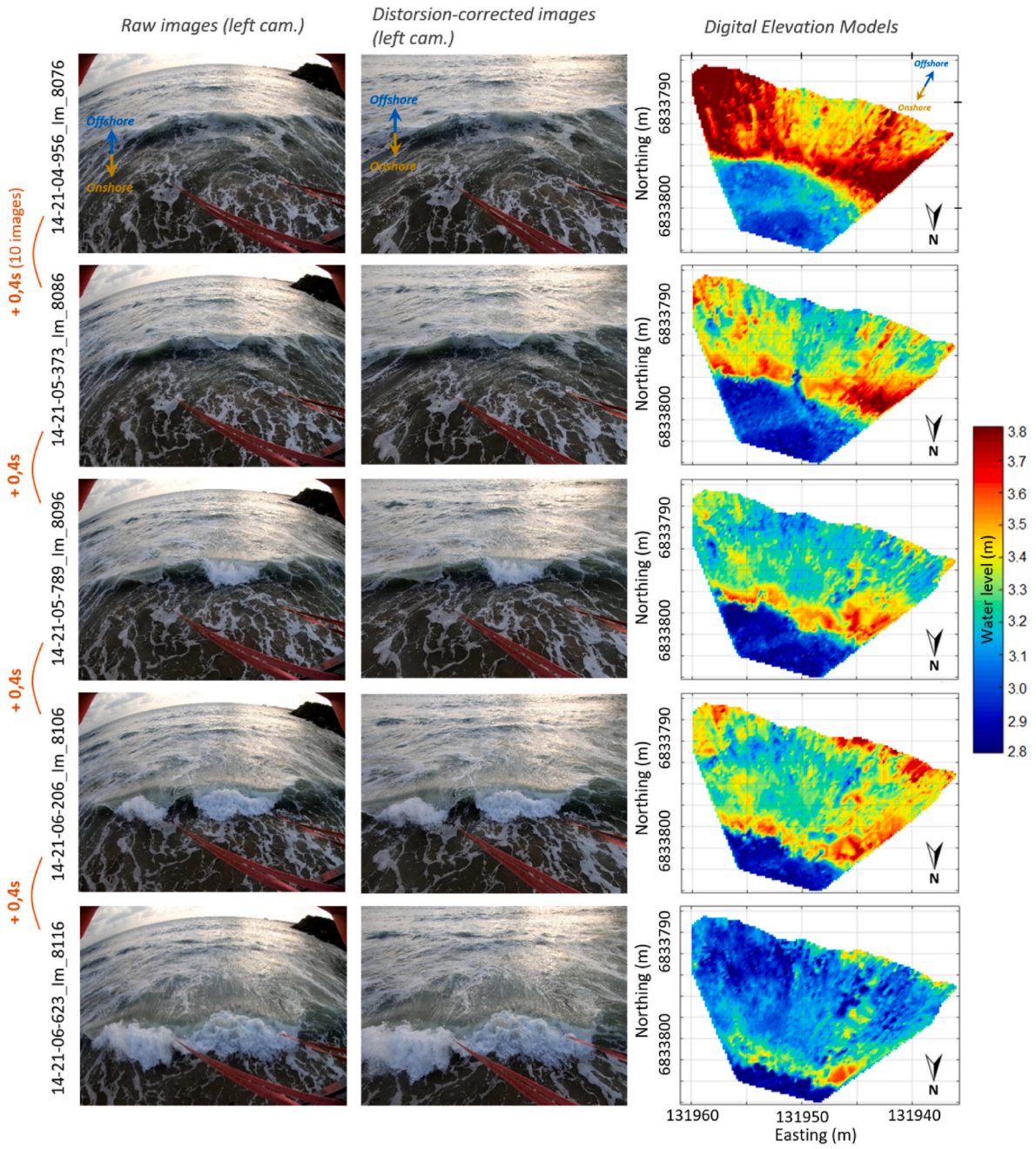

Fig. 7. Series of five raw images (first column) of a breaking wave, corresponding images corrected of geometrical distortions (second column), and the resulting stereo-GoPro DEMs (third column) in RGF 93 - Lambert 93 cartographic coordinates. The time step between images is 0.4 s.

pressure sensor by ~0.3 m). This difference may arise from instruments not measuring the same thing when it comes to monitoring breaking waves (Baker et al., 2023), due for instance to the presence of foam at the water surface.

In Fig. 9, we present scatter plots of the comparisons between the free-surface elevations measured independently by the three measuring devices. Again, the evaluation concerns 25 min of recording at a sampling rate of 4.8 Hz, corresponding to n = 7173 time-wise comparisons. Statistics derived from the comparisons are reported in Table I. It shows a very good agreement between the LiDAR and the pressure sensor, with a correlation coefficient R = 0.95 ($p < 0.05$) and a mean vertical bias/standard deviation of the differences (SDE) both equal to 0.08 m (RMSE = 0.11 m). We observe that differences are becoming progressively larger as free-surface elevation increases, with linear regression indicating an under evaluation of large waves by the pressure sensor in comparison to LiDAR. Comparing stereo-GoPro with the pressure sensor and LiDAR show similar tendencies and statistics, with R = 0.79 ($p < 0.05$) and SDE = 0.16 m and 0.15 m, respectively. The mean error between stereo-GoPro and the pressure sensor amounted to 0.1 m, for only 0.02 m in comparison to LiDAR. Likewise, Fig. 9 shows an underestimation of large waves with stereo-GoPro, which is observed in comparisons with both the pressure sensor and the LiDAR. The maximum error was computed to be 0.93 m (0.74 m) between stereo-GoPro (LiDAR) and the pressure sensor.

To spatialize the assessment of the quality of the stereo-video reconstruction, stereo-video was compared with LiDAR for all 16 beams at a given time (Fig. 10). A distance measurement (point to mesh) was carried out using the software CloudCompare® between corresponding stereo-GoPro DEMs and LiDAR point clouds. This operation cannot be automated, and for this reason, was carried out only for a

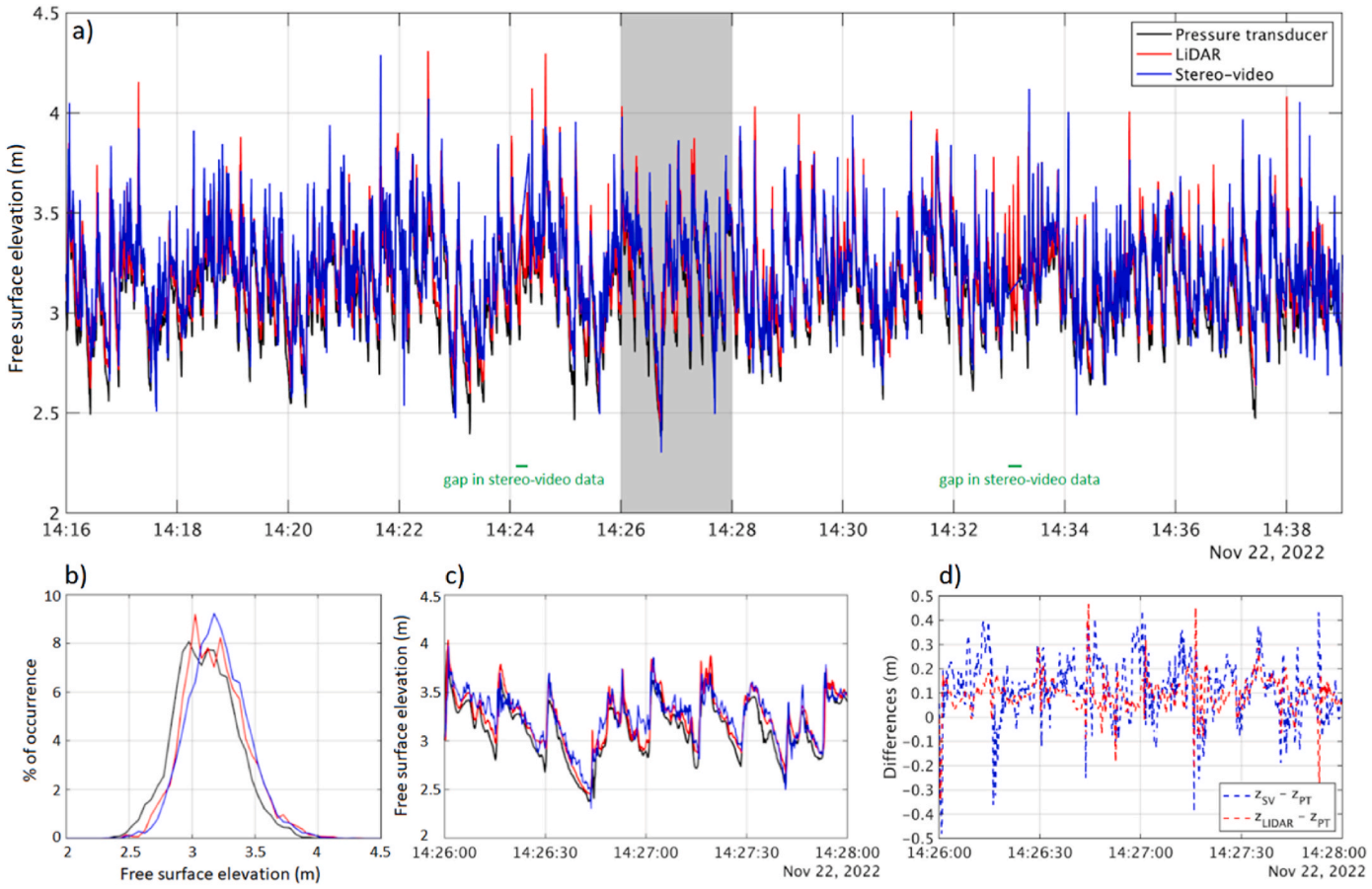

Fig. 8. a) Free-surface evolution over 25 min at High Tide at the location of the pressure sensor as determined by the three measuring devices used during the experiment (pressure sensor, LiDAR and stereo-GoPro). b) Probability Distribution of free-surface elevation for the three instruments. Close-up view on 2 min, with c) free-surface elevation and d) differences between stereo-video (LiDAR) and the pressure sensor, respectively.

limited number of stereo-GoPro DEMs. Fig. 10 shows the comparison between stereo-GoPro and LiDAR for a breaking wave measured at 14:21:05 UTC time and considered typical of what was observed throughout the experiment. The calculation of point-to-mesh distances (Fig. 10c) shows a mean deviation of −0.13 m (the stereo-video DEM being on average above LiDAR points) and a standard deviation of 0.10 m.

Power spectral densities calculated from the detrended water level time-series for the three measurement techniques are presented in Fig. 11. Similar to what was observed previously, it shows a very good agreement overall between the LiDAR and the pressure sensor. Detailed observations suggest a slightly lower peak for the pressure sensor in the gravity band, and a slightly higher peak in the infragravity band, which is corroborated by wave parameters estimated using spectral moments methods (Table II). Stereo-GoPro results are characterized by a lower peak in the gravity band and larger values in the infragravity band. Besides, Fig. 11 shows accentuated noise at high frequencies in stereo-GoPro data (e.g., for $f > 0.5$ Hz).

In Table II, we present the spectral wave parameters determined using the free-surface timeseries for the three measuring devices presented in Fig. 8, as well as their relative differences in comparison to LiDAR taken as reference. It shows that LiDAR and pressure sensor data are very close to each other, both in terms of wave height (Hm0 and Hm0-IG) and wave periods (Tm02, Tp and Tm02-IG), with a maximum relative difference found to be ∼4% on Hm0-IG and less than 1.2% error on other parameters estimated. The significant wave height in the gravity band (Hm0) obtained using LiDAR was larger than those estimated using the pressure sensor and stereo-video, which follows previous observations (e.g., Figs. 8 and 9). Table II shows that stereo-video resulted in reduced Hm0 and Tm02, but an increased Hm0-IG, with relative differences up to 12.5%.

7. Discussion

This study has presented a field comparison between remote-sensing techniques (stereo-video and LiDAR) and pressure sensors for measuring nearshore waves. The instruments were deployed in the surf zone at a macrotidal field site (Porsmilin) during energetic conditions, with comparisons performed at high tide when waves were the largest. We showed that stereo-video and low-cost sensors such as GoPro cameras can produce acceptable results, both for reconstructing the free-surface evolution (RMSE = 0.15 m in comparison with LiDAR) and for estimating spectral wave parameters (e.g., maximum relative error of 12.5% on Hm0). However, there remains various challenges encountered associated with the measurement of a dynamic water surface and to the complex but necessary task of assessing the quality of the data obtained using dissimilar instruments, which we discuss hereafter. We further explore potential technical enhancements for the stereo-GoPro system and its applicability to other hydrodynamic scenarios.

7.1. Challenges associated with water-surface measurements and data quality evaluation

Using GoPro cameras for reliable water surface measurements provided several challenges, essentially related to the short focal length and the associated large optical distortion in images. Camera calibration has the potential to estimate and correct image distortion. In this study using a checkerboard, both radial and tangential distortion coefficients were

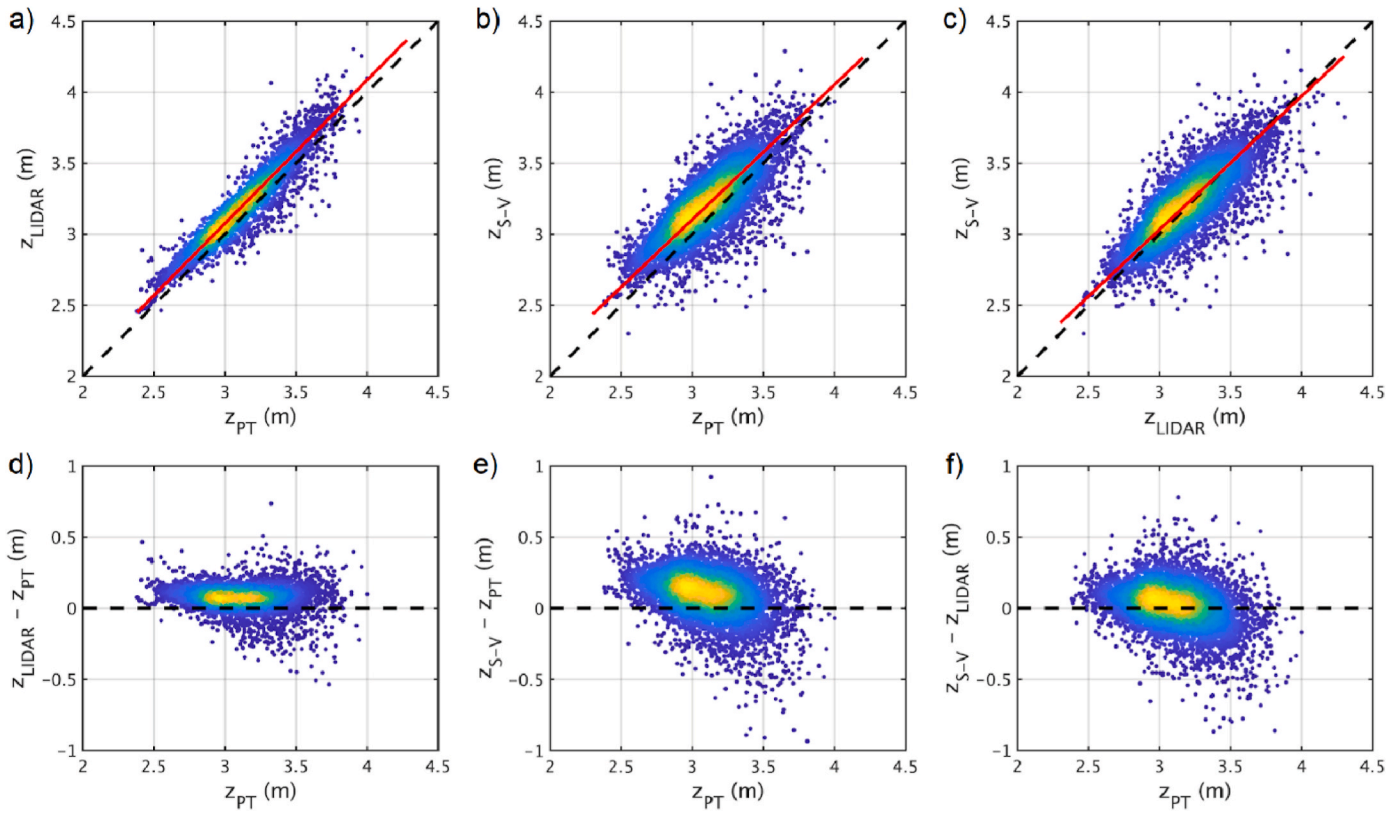

Fig. 9. Scatter plots of (a,b,c) the comparisons between the free-surface elevations (z) measured independently by the three measuring devices (1:1 relation is shown by the dashed line, while the red line is the linear regression), and (d,e,f) the differences between measurements and the free-surface elevation estimated using the pressure sensor taken as reference. (For interpretation of the references to color in this figure legend, the reader is referred to the Web version of this article.)

Table 1
Error statistics estimated from the comparisons between the free-surface elevation timeseries estimated using the pressure sensor (Z_{PT}), the Velodyne LiDAR (Z_{LiDAR}) and stereo-GoPro ($Z_{S\text{-}V}$). Comparisons were performed over 25 min of recording at a sampling rate of 4.8 Hz.

	Z_{LiDAR} - Z_{PT}	$Z_{S\text{-}V}$ - Z_{PT}	$Z_{S\text{-}V}$ - Z_{LiDAR}
Correlation coefficient R	0.95	0.79	0.79
ME (m)	0.08	0.10	0.02
SDE (m)	0.08	0.16	0.15
RMSE (m)	0.11	0.18	0.15
Maximum unsigned error (m)	0.74	0.93	1.04

calculated. Common to stereo-photogrammetric applications using a pre-calibration approach for estimating intrinsic and extrinsic parameters, we paid particular attention not to alter the system geometry when handling it between calibration, performed on site, and installation on the tower, so that calibration parameters remained valid. Nevertheless, calibration errors (reprojection and rectification errors) were estimated to be mostly above 1 pixel (Fig. 4), the latter being considered in previous work as the threshold below which optimal conditions for matching points in stereo images are generally met, limiting the risk of introducing additional errors due to calibration (e.g., Bertin et al., 2015).

Inaccurate calibration parameters can result in measurement artifacts taking the shape of a dome or bowl in 3D reconstructions, generally referred to as the 'dome effect' (e.g., James et al., 2012; James and Robson, 2014). We believe such deformations were present in our stereo-GoPro reconstructions, explaining in part the differences we observed between instruments (e.g., Fig. 10). However, this effect could not be directly evidenced through comparisons with pressure sensor and LiDAR data, a reason being the limited surface coverage. To evidence geometric deformations in photogrammetry requires spatial comparisons with ideally a concurrent deformation-free DEM or a large number of well-distributed and high-quality validation points (Bertin et al., 2022a), which is particularly challenging in application to a dynamic surface such as water waves.

To assess the presence and magnitude of geometric deformations in stereo-GoPro data, we had recourse to an alternative and tentative strategy, which assumes that over a long duration (e.g., several minutes or more), temporally averaging at-a-point elevations produces a flat water surface (i.e., propagating waves cancel out). This same strategy is used in WASS to estimate the mean water planes from which stereo-video data are transformed to produce consistent and horizontal water surfaces (Bergamasco et al., 2017). We note however that in the near-shore zone, water surface deformations may be occurring, e.g., due to the presence of wave setup and infragravity waves (Benetazzo et al., 2012). Hard to estimate a priori, they will naturally be present in the elevation maps and cannot be distinguished from the dome effect. For instance, our combined measurements estimated a significant wave height (Hm0) in the infragravity band of 0.35 m (cf. Table II), which is commensurate with the magnitude of the deformations presented in Fig. 12. The dome effect suggested by Fig. 12 reaches a total magnitude as high as 0.5 m and is almost symmetrical along the camera viewing axis, which would be anticipated for this type of 3D photogrammetric error. It is questionable however whether the dome was correctly estimated since the corrected water-surface elevations still indicate the presence of a small deformation in place of the dome, which could otherwise be due to a small wave (higher-harmonic wave?) in front of the larger breaking wave evidenced at the rear of the DEM. The dome effect was previously reported in SfM photogrammetry using GoPros (e.g., Li et al., 2018), with a magnitude commensurate with the one estimated in this study. Potential avenues of improvement include increasing the number of calibration images, with for instance previous

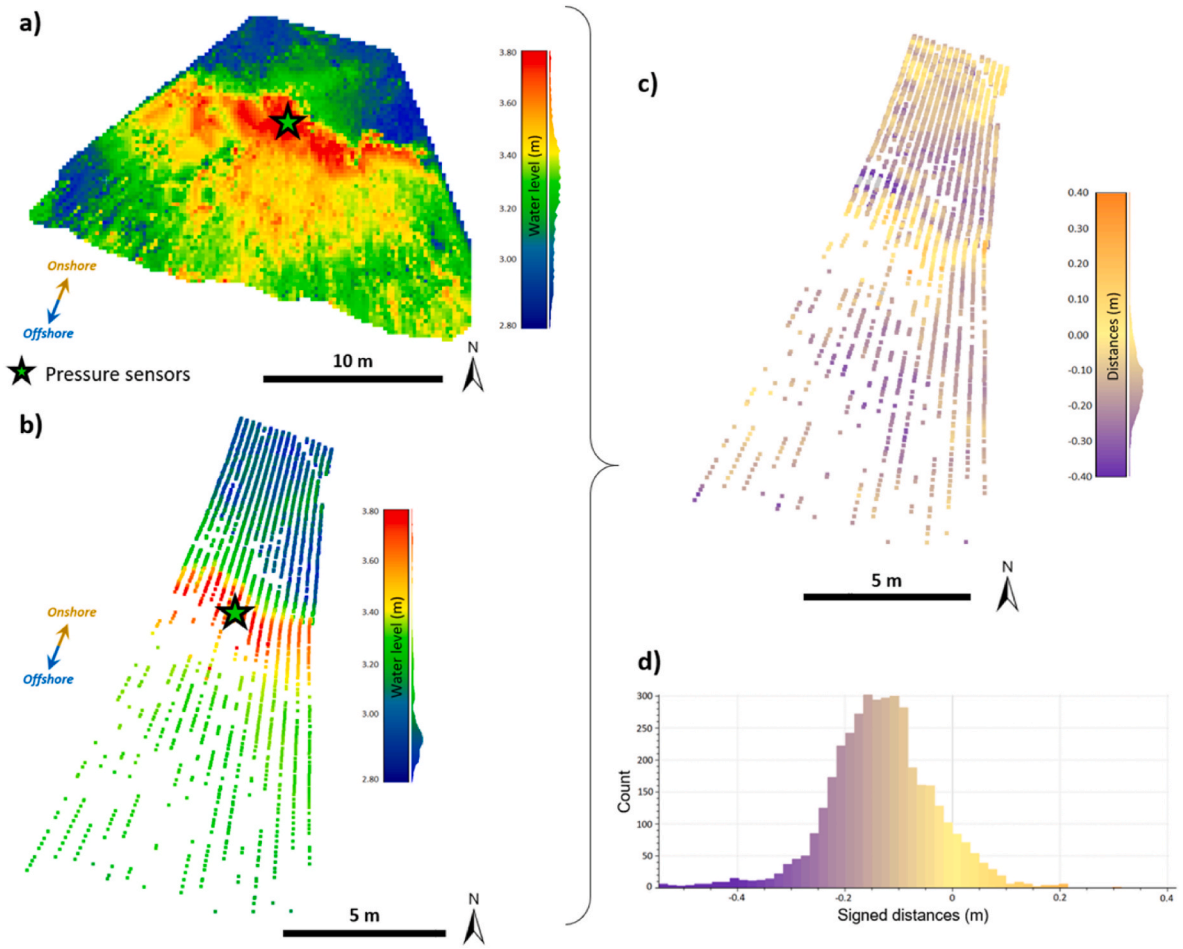

Fig. 10. Spatial inter-comparison, at a given time (14:21:05 UTC time), between the water surface measured independently by stereo-GoPro and multi-beam LiDAR. a) and b) show the stereo-GoPro and LiDAR DEM and point cloud, respectively. The location of the pressure transducer is indicated by the green star. c) Point to mesh differences between LiDAR and stereo-GoPro. d) Probability distribution of the differences. (For interpretation of the references to color in this figure legend, the reader is referred to the Web version of this article.)

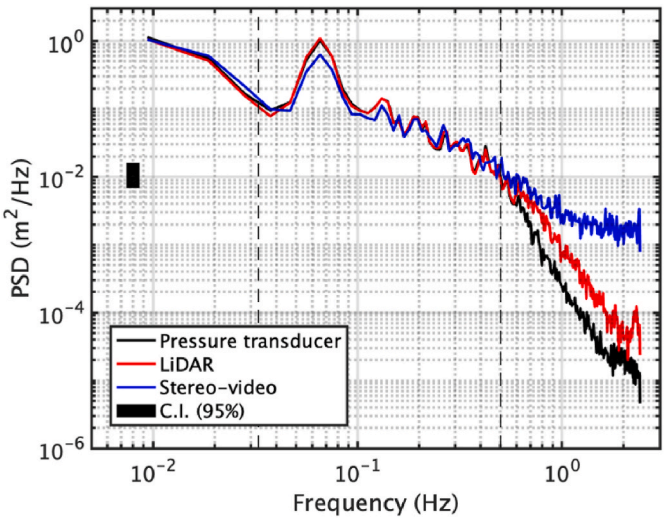

Fig. 11. Welch's Power Spectral Densities (PSDs) estimated from the detrended water level timeseries (burst duration = 20 min, nfft = 512, overlap = 50%, confidence level C.I. = 95%). Vertical dashed lines correspond to the bounding frequencies for calculating gravity and infragravity wave parameters using the spectral moments' methods.

Table 2
Spectral wave parameters estimated from the detrended water surface timeseries (burst duration = 20 min, nfft = 512, overlap = 50%) and their relative difference in comparison to LiDAR. IG stands for infragravity.

	Pressure sensor	LiDAR	Stereo-GoPro
Hm0 (m)	0.81 (−1.13 %)	0.82	0.72 (−12.53 %)
Hm0_IG (m)	0.33 (3.92 %)	0.32	0.35 (10.79 %)
Tm02 (s)	6.11 (−1.07 %)	6.18	5.35 (−12.41 %)
Tp(s)	15.24 (0 %)	15.24	15.24 (0 %)
Tm02_IG (s)	46.95 (0.07 %)	46.92	46.26 (−1.39 %)

stereo-video applications using calibration images in excess of 50 (Benetazzo et al., 2012; Guimarães et al., 2020). Besides, camera calibration could be done in the laboratory or a sheltered environment, prior to or after field deployment to limit the risk of wind moving the checkerboard and affecting extrinsic parameters calculation. This is the strategy favored in WASS, whereby extrinsic parameters are directly estimated from water surface images, leaving determination of intrinsic parameters only with a chequerboard. This could limit the eventuality of inaccurate extrinsic parameters, with limited improvement on the dome effect however, as it is essentially caused by inaccurate intrinsic parameter estimation (e.g., focal length and distortion coefficients).

Further improvements would otherwise necessitate adopting higher-quality optics, as this is a main factor controlling photogrammetric quality (Mosbrucker et al., 2017), at the drawback however of cost

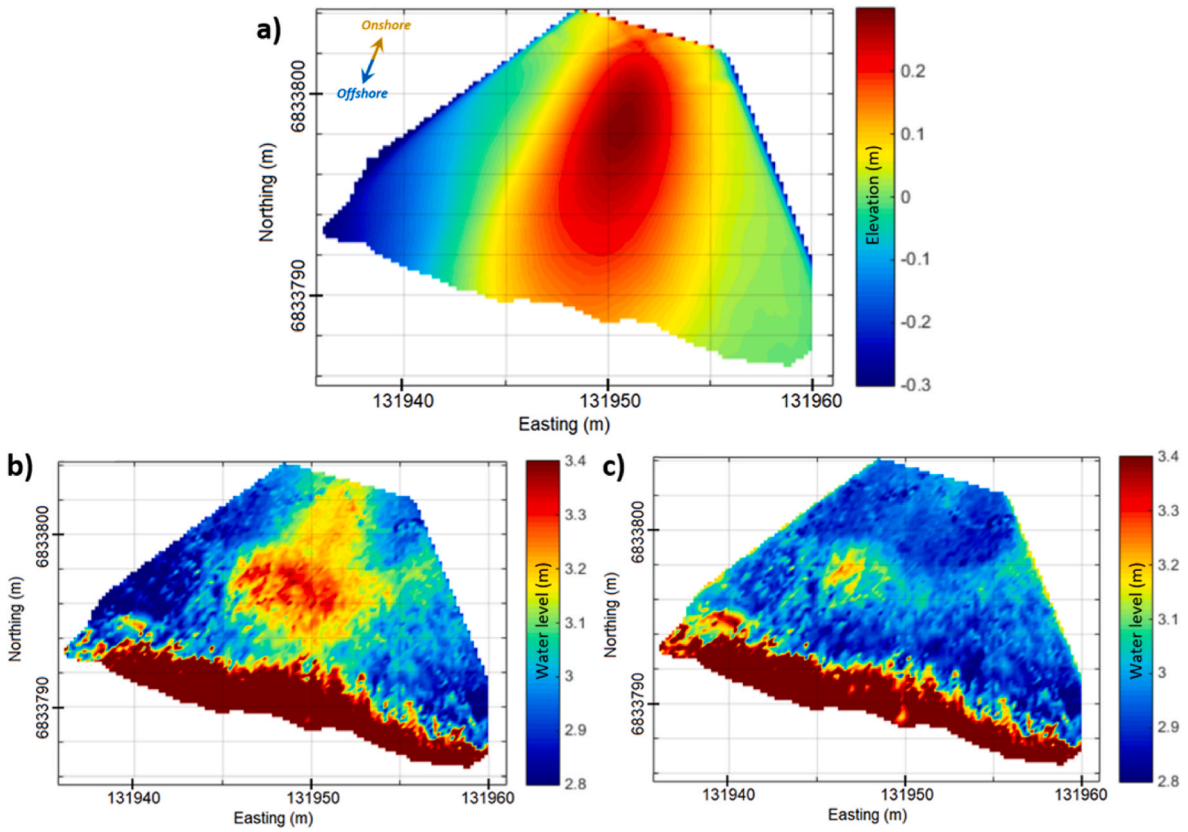

Fig. 12. a) Estimation of the dome effect by averaging the DEMs to retain only a low-frequency signal. Example of a water-surface DEM before (b) and after (c) dome correction by subtracting the average dome surface (a).

increases. Bowl-corrected stereo-GoPro DEMs were used in point-wise comparison (not shown) with water level time-series issued from the pressure transducer and LiDAR, providing no significant change.

Data georeferencing, which facilitated instrument comparisons and enables draping water surfaces above a measured bathymetry, further represented a challenging task that was error-prone. Taking advantage of the large tidal range at the test site, GCPs were deployed at low tide and surveyed independently with RTK-GNSS. Ideally, GCPs should be distributed evenly across the entire measurement area to ensure a well-constrained solution, which could not be achieved for this test using only five GCPs.

Despite these caveats, the evaluation of stereo-GoPro data quality with the pressure sensor and LiDAR showed that satisfactory results can nevertheless be obtained. Accuracy, estimated with the mean error in comparison to the pressure sensor taken as ground truth, was similar to LiDAR (Fig. 8 and Table II). In this regard, the dynamic water level estimated using LiDAR and stereo-GoPro was found to be nearly 0.1 m above pressure sensor estimates (Table I). This suggests the superiority of optical methods that directly measure the water surface, unlike the indirect estimation done by pressure sensors, for which setting the mean water level can be impacted by atmospheric pressure correction (cf. section 3.2). Yet, still in comparison with the pressure sensor, LiDAR was found twice as precise as stereo-GoPro, shown by SDE = 0.08 m and 0.16 m, respectively. These comparisons raised the question however of whether all three instruments measured the same thing when it comes to breaking waves, with previous studies indicating disparate results between optical methods and pressure measurements in the presence of foam and aerated water (Baker et al., 2023; Martins et al., 2017). In particular, considering that the reconstruction using linear theory underestimates the steepness of waves, this would explain the larger differences observed at wave crests (Fig. 8).

Bearing in mind that photogrammetric data quality depends on a number of factors, primarily camera specifications and measurement distances, hence ground sampling distance, the detailed error assessment presented in this study suggests that stereo-GoPro performance is commensurate with field applications presented in previous work. Guimarães et al. (2020) provided a summary of different stereo-video applications using high-quality cameras and optics from offshore platforms (ex. La Jument lighthouse). Not disposing of independent data for assessing measurement quality, they reported a theoretical RMSE whose maximum value was 0.1 m. Similarly, De Vries et al. (2011) presented a field application of stereo-video at Scheveningen pier. In the absence of ground truth data, they concluded that accuracy (not mentioning what error metric this is) is conservatively assumed to be below 0.1 m. Closer to our application, using two smartphones as a stereo-setup Vieira et al. (2020) reported RMSE of 0.1–0.12 m in comparison with a pressure sensor. It is important to note that these different applications did not have recourse to data georeferencing, and error evaluation was only point-wise, potentially limiting the total error rate in comparison to our study. Previous work showed that improved quality can be obtained in the controlled conditions provided by laboratory flumes, with Baker et al. (2023) in particular reporting centimetric RMSE (of the order of 0.02–0.075 m) in comparison with a pressure sensor and a LiDAR. Furthermore, as in the study by Baker et al. (2023), our inter-comparison shows differences mainly at wave crests and troughs. This can be due to the spatial sampling of the measurements or to interpolation effects on the stereo-video DEM. Some of the discrepancies can also be explained by the fact that pressure sensors do not directly measure the water surface, which is obtained by inversion, without considering any surface foam effects. This issue highlights the difficulties of assessing the quality of a method and the limits of intercomparing.

Finally, previous studies employing high-quality cameras (e.g., Malila et al., 2022) did not observe high-frequency noise in stereo reconstructions (Fig. 11), suggesting that it could result from the

extraction of images from compressed video formats (e.g., MP4), reducing image quality.

7.2. Potential of the system

The primary advantage of a low-cost system is its affordability. It is anticipated that reduced costs could allow either for the deployment of monitoring systems at multiple sites simultaneously or for the duplication of measurements at a given site to increase spatial coverage and/or evaluate the replicability of the results. Utilizing widespread devices, such as GoPro cameras, already mass-produced, significantly reduced the overall cost of the monitoring system used in this study. Furthermore, these devices can be easily replaced in the event of damage or loss, a possibility in hazardous water environments such as the coastal zone or river systems.

The versatility of the stereo-GoPro system enables it to accommodate changing monitoring needs or site specificity. Previously, Stereo-GoPro was successfully deployed at another study site, in different meteorological and hydrodynamic conditions (measurements were carried out in the swash zone, with wave heights of a few tens of centimeters, during a sunny day - Jaud et al., 2022). Even though a study assessing the effect of ambient conditions on stereo-video performance has yet to be conducted, our tests suggest that sunlight (particularly sunglint effects) and water transparency (detection of the seabed rather than the water surface) can be obstacles to free-surface and water wave measurements. For future experiments, the use of polarizing filters seems particularly promising to reduce glare from the sea surface, improving image contrast and stereo-matching performance, in case challenging lighting conditions prevail. This could potentially allow measuring water surfaces under varied illuminations, providing the ability to measure throughout the day as illumination will naturally vary without necessarily having the possibility to change camera and setup orientation. Additional technical improvements of the system remain also to be tested. It would be interesting, for example, to improve the autonomy of the system, either by increasing the recording time (batteries, storage media, etc.) or by setting up a more automated camera synchronization system. For future surveys, we plan to improve the hydrodynamics of the tower by replacing the mooring straps with cables, enhancing the stability of the whole system in energetic conditions while reducing the occlusion zone produced by straps, which were visible in the images. Certain geometric parameters of the system could also be adapted (height of tower, baseline between cameras, changing the camera model, etc.). For example, in the event of larger waves, it is conceivable to change the orientation of the cameras (viewing azimuth, angle of incidence) to avoid wave troughs being masked by wave crests.

The inter-comparison of stereo-video with a pressure transducer and a multi-beam LiDAR presented in this study can be used to highlight the potential and limitations of stereo-video method with respect to the other two techniques. Importantly, stereo-video makes it possible to generate spatially continuous data, unlike the LiDAR profiler, together with a larger surface coverage, particularly alongshore. This longshore coverage may prove beneficial in future work for monitoring wave spatial variability such as for short-crested waves. In addition, the fact that stereo-video data not only comprise a point cloud or DEM, but also images, can be helpful to interpret the elevation maps produced (e.g., as in Fig. 7).

In terms of stereo-video potential and data analysis, wave non-linearities are shown to be among the main drivers of sediment transport (e.g., Masselink et al., 2016; Rocha et al., 2017; Van Der A et al., 2010), becoming non-negligible during wave shoaling and breaking processes. This results in a particular wave shape, known as wave asymmetry and skewness, driving the temporal variability of bed shear stress in shallow water environments. In future work, it will be necessary to explore these non-linearities using the 4D datasets produced using stereo-video and LiDAR.

Finally, the system's versatility means it can also be used in other environments, whether outdoor or in the laboratory, as long as the water surface has sufficient texture for stereo-restitution. Despite limited studies so far, stereo-video shows significant potential for use in river systems, with for instance Li et al. (2019) using it to generate ortho-rectified images of the surface of a mountain river in order to apply Particle Image Velocimetry methods. To allow a large uptake of the technique, further research is necessary to assess in more detail the effect of acquisition configurations and ambient conditions on stereo-video performance.

8. Conclusion

This study presents an inter-comparison carried out at a coastal field site in Northwest France (Porsmilin beach) for measuring nearshore waves, using concurrently a pressure sensor, a 16-beam LiDAR and a stereo-video system, during an energetic wave event akin to what was considered a moderate storm. Measurements were carried out at high tide, and the paper has presented a comparison of the three wave measuring devices over 25 min of recording.

The stereo-video system is based on low-cost devices, making use of two GoPro cameras and a purpose-built processing workflow within which essential steps (e.g., stereo calibration using a 2D checkerboard and 3D reconstruction) are performed with solutions already available (e.g., the stereo camera calibration toolbox and MicMac software). These were completed by in-house methods for synchronizing cameras, georeferencing the data and preparing DEMs from point clouds, which comprises filtering outlier points and cropping to a consistent region of interest according to a minimum density threshold.

This study demonstrated that stereo-video with affordable sensors like GoPro cameras proved effective in reconstructing free-surface evolution, with an RMSE of 0.15 m compared to LiDAR and 0.18 m with the pressure sensor. It also provided reasonable estimates of spectral wave parameters, with relative errors constantly below 13%. Nevertheless, challenges persist in field measurements of dynamic water surfaces and in evaluating data quality when using diverse instruments. Our evaluation suggested that complex 3D deformations can be present in stereo-video data, resulting from inaccurate estimation of camera calibration parameters. Given the versatility of the system and that several opportunities for improvement exist, this method opens up new doors to obtain high-frequency DEMs of a (textured) water surface at low cost. This presents exciting opportunities for extracting wave parameters in coastal areas, but also for other field of applications.

CRediT authorship contribution statement

Marion Jaud: Writing – review & editing, Writing – original draft, Visualization, Validation, Methodology, Investigation, Conceptualization. **Stéphane Bertin:** Writing – review & editing, Writing – original draft, Visualization, Validation, Software, Methodology, Investigation, Formal analysis, Conceptualization. **Emmanuel Augereau:** Writing – review & editing, Visualization, Validation, Software, Methodology, Investigation, Data curation, Conceptualization. **France Floc'h:** Writing – review & editing, Software, Project administration, Methodology, Funding acquisition, Conceptualization.

Data availability

The DEMs generated by the stereo-video method described in this article are available at this DOI: https://doi.org/10.5281/zenodo.11072710.

Declaration of competing interest

The authors declare that they have no known competing financial interests or personal relationships that could have appeared to influence the work reported in this paper.

Acknowledgments

This study has been carried out in the framework of the WEST project (Natural Breaking WavEs and Sediment Transport during beach recovery - ANR-20-CE01-009) granted by the Agence Nationale pour la Recherche (ANR).

The authors are also grateful to ISblue project, the Interdisciplinary graduate school for the blue planet (ANR-17-EURE-0015) for its financial support in funding the internship of Aelaïg Cournez.

We would like to thank Charles Poitou for his assistance in the field. This paper was edited by George Vosselman and reviewed by Falk Feddersen and two anonymous referees, whose help is gratefully acknowledged.

References

Baker, C.M., Moulton, M., Palmsten, M.L., Brodie, K., Nuss, E., Chickadel, C.C., 2023. Remotely sensed short-crested breaking waves in a laboratory directional wave basin. Coast. Eng. 183, 104327. https://doi.org/10.1016/j.coastaleng.2023.104327.

Belmont, M.R., Horwood, J.M.K., Thurley, R.W.F., Baker, J., 2007. Shallow angle wave profiling lidar. J. Atmos. Ocean. Technol. 24 (1), 1150–1156. https://doi.org/10.1175/JTECH2032.

Benetazzo, A., Fedele, F., Gallego, G., Shih, P.-C., Yezzi, A., 2012. Offshore stereo measurements of gravity waves. Coast. Eng. 64, 127–138. https://doi.org/10.1016/j.coastaleng.2012.01.007.

Bergamasco, F., Torsello, A., Sclavo, M., Barbariol, F., Benetazzo, A., 2017. WASS: an open-source pipeline for 3D stereo reconstruction of ocean waves. Comput. Geosci. 107, 28–36. https://doi.org/10.1016/j.cageo.2017.07.001.

Bertin, S., Friedrich, H., Delmas, P., Chan, E., Gimel'farb, G., 2015. Digital stereo photogrammetry for grain-scale monitoring of fluvial surfaces: error evaluation and workflow optimisation. ISPRS J. Photogrammetry Remote Sens. 101, 193–208. https://doi.org/10.1016/j.isprsjprs.2014.12.019.

Bertin, S., Jaud, M., Delacourt, C., 2022a. Assessing DEM quality and minimizing registration error in repeated geomorphic surveys with multi-temporal ground truths of invariant features: application to a long-term dataset of beach topography and nearshore bathymetry. Earth Surf. Process. Landforms 5436. https://doi.org/10.1002/esp.5436.

Bertin, S., Floc'h, F., Le Dantec, N., Jaud, M., Cancouët, R., Franzetti, M., Cuq, V., Prunier, C., Ammann, J., Augereau, E., Lamarche, S., Belleney, D., Rouan, M., David, L., Deschamps, A., Delacourt, C., Suanez, S., 2022b. A long-term dataset of topography and nearshore bathymetry at the macrotidal pocket beach of Porsmilin, France. Sci. Data 9, 79. https://doi.org/10.1038/s41597-022-01170-3.

Bishop, C.T., Donelan, M.A., 1987. Measuring waves with pressure transducers. Coast. Eng. 11, 309–328. https://doi.org/10.1016/0378-3839(87)90031-7.

Blenkinsopp, C.E., Mole, M.A., Turner, I.L., Peirson, W.L., 2010. Measurements of the time-varying free-surface profile across the swash zone obtained using an industrial LIDAR. Coast. Eng. 57, 1059–1065. https://doi.org/10.1016/j.coastaleng.2010.07.001.

Bonneton, P., Lannes, D., 2017. Recovering water wave elevation from pressure measurements. J. Fluid Mech. 833, 399–429. https://doi.org/10.1017/jfm.2017.666.

Brodie, K.L., Raubenheimer, B., Elgar, S., Slocum, R.K., McNinch, J.E., 2015. Lidar and pressure measurements of inner-surfzone waves and setup. J. Atmos. Ocean. Technol. 32, 1945–1959. https://doi.org/10.1175/JTECH-D-14-00222.1.

Bruder, B.L., Brodie, K.L., 2020. CIRN quantitative coastal imaging toolbox. SoftwareX 12, 100582. https://doi.org/10.1016/j.softx.2020.100582.

Bulleri, F., Cucco, A., Dal Bello, M., Maggi, E., Ravaglioli, C., Benedetti-Cecchi, L., 2018. The role of wave-exposure and human impacts in regulating the distribution of alternative habitats on NW Mediterranean rocky reefs. Estuar. Coast Shelf Sci. 201, 114–122. https://doi.org/10.1016/j.ecss.2016.02.013.

Camenen, B., Larroudé, P., 2003. Comparison of sediment transport formulae for the coastal environment. Coast. Eng. 48, 111–132. https://doi.org/10.1016/S0378-3839(03)00002-4.

Castelle, B., Scott, T., Brander, R.W., McCarroll, R.J., 2016. Rip current types, circulation and hazard. Earth Sci. Rev. 163, 1–21. https://doi.org/10.1016/j.earscirev.2016.09.008.

Chella, M.A., Tørum, A., Myrhaug, D., 2012. An overview of wave impact forces on offshore wind turbine substructures. Energy Proc. 20, 217–226. https://doi.org/10.1016/j.egypro.2012.03.022.

Colvin, J., Lazarus, S., Splitt, M., 2020. Extracting nearshore wave properties from video: a new method for coastal estuaries. Estuar. Coast Shelf Sci. 246, 107053. https://doi.org/10.1016/j.ecss.2020.107053.

Cowley, D., Harris, D.L., 2023. Wave-driven sediment transport potential on a tropical coast: implications for the northeastern Australian sediment budget. Mar. Geol. 463, 107104. https://doi.org/10.1016/j.margeo.2023.107104.

De Vries, S., Hill, D.F., De Schipper, M.A., Stive, M.J.F., 2011. Remote sensing of surf zone waves using stereo imaging. Coast. Eng. 58, 239–250. https://doi.org/10.1016/j.coastaleng.2010.10.004.

Dehouck, A., Dupuis, H., Sénéchal, N., 2009. Pocket beach hydrodynamics: the example of four macrotidal beaches, Brittany, France. Mar. Geol. 266, 1–17. https://doi.org/10.1016/j.margeo.2009.07.008.

Feddersen, F., Fincham, A.M., Brodie, K.L., Young, A.P., Spydell, M.S., Grimes, D.J., Pieszka, M., Hanson, K., 2023. Cross-shore wind-induced changes to field-scale overturning wave shape. J. Fluid Mech. 958, A4. https://doi.org/10.1017/jfm.2023.40.

Feddersen, F., Marques, O.B., MacMahan, J.H., Grenzeback, R.L., 2024. Estimating directional wave spectra properties in nonbreaking waves from a UAS-mounted multibeam lidar. J. Atmos. Ocean. Technol. 41, 515–530. https://doi.org/10.1175/JTECH-D-23-0129.1.

Fiedler, J.W., Kim, L., Grenzeback, R.L., Young, A.P., Merrifield, M.A., 2021. Enhanced surf zone and wave runup observations with hovering drone-mounted lidar. J. Atmos. Ocean. Technol. 38, 1967–1978. https://doi.org/10.1175/JTECH-D-21-0027.1.

Grasso, F., Michallet, H., Barthélemy, E., 2011. Sediment transport associated with morphological beach changes forced by irregular asymmetric, skewed waves. J. Geophys. Res. 116, C03020. https://doi.org/10.1029/2010JC006550.

Guimarães, P.V., Ardhuin, F., Bergamasco, F., Leckler, F., Filipot, J.-F., Shim, J.-S., Dulov, V., Benetazzo, A., 2020. A data set of sea surface stereo images to resolve space-time wave fields. Sci. Data 7, 145. https://doi.org/10.1038/s41597-020-0492-9.

Haller, M.C., Lyzenga, D.R., 2003. Comparison of radar and video observations of shallow water breaking waves. IEEE Trans. Geosci. Rem. Sens. 41, 832–844. https://doi.org/10.1109/TGRS.2003.810695.

Harry, M., Zhang, H., Lemckert, C., Colleter, G., 2010. 3D spatial definition of a water surface. In: Proceedings of the Ninth (2010) ISOPE Pacific/Asia Offshore Mechanics Symposium. Presented at the ISOPE Pacific/Asia Offshore Mechanics Symposium. The International Society of Offshore and Polar Engineers, Busan, Korea.

Harry, M., Zhang, H., Lemckert, C., Colleter, G., Blenkinsopp, C., 2018. Observation of surf zone wave transformation using LiDAR. Appl. Ocean Res. 78, 88–98. https://doi.org/10.1016/j.apor.2018.05.015.

Hom-ma, M., Horikawa, K., Komori, S., 1966. Response characteristics of underwater wave gauge. Coast. Eng. Jpn. 9, 45–54. https://doi.org/10.1080/05785634.1966.11924671.

Horwood, J.M.K., Thurley, R.W.F., Belmont, M.R., Baker, J., 2005. Shallow angle LIDAR for wave measurement. Europe Oceans 2005. Presented at the Oceans 2005 - Europe 2, 1151–1154. https://doi.org/10.1109/OCEANSE.2005.1513221. IEEE, Brest, France.

James, L.A., Hodgson, M.E., Ghoshal, S., Latiolais, M.M., 2012. Geomorphic change detection using historic maps and DEM differencing: the temporal dimension of geospatial analysis. Geomorphology 137, 181–198. https://doi.org/10.1016/j.geomorph.2010.10.039.

James, M.R., Robson, S., 2014. Mitigating systematic error in topographic models derived from UAV and ground-based image networks: mitigating systematic error in topographic models. Earth Surf. Process. Landforms 39, 1413–1420. https://doi.org/10.1002/esp.3609.

Jaud, M., Bertin, S., Augereau, E., Poitou, C., Cournez, A., Fritsch, N., Floc'H, F., 2022. Développement et évaluation d'un système de stéréo-vidéo pour la mesure de vagues en zone de déferlement. In: XVIIèmes Journées, Chatou. Presented at the Journées Nationales Génie Côtier - Génie Civil, Editions Paralia, pp. 461–474. https://doi.org/10.5150/jngcgc.2022.048.

Leckler, F., Ardhuin, F., Peureux, C., Benetazzo, A., Bergamasco, F., Dulov, V., 2015. Analysis and interpretation of frequency–wavenumber spectra of young wind waves. J. Phys. Oceanogr. 45, 2484–2496. https://doi.org/10.1175/JPO-D-14-0237.1.

Li, W., Bertin, S., Friedrich, H., 2018. Combining Structure from Motion and close-range stereo photogrammetry to obtain scaled gravel bar DEMs. Int. J. Rem. Sens. 39, 9269–9293. https://doi.org/10.1080/01431161.2018.1530809.

Li, W., Liao, Q., Ran, Q., 2019. Stereo-imaging LSPIV (SI-LSPIV) for 3D water surface reconstruction and discharge measurement in mountain river flows. J. Hydrol. 578, 124099. https://doi.org/10.1016/j.jhydrol.2019.124099.

Malila, M.P., Thomson, J., Breivik, Ø., Benetazzo, A., Scanlon, B., Ward, B., 2022. On the groupiness and intermittency of oceanic whitecaps. J. Geophys. Res. Oceans 127, e2021JC017938. https://doi.org/10.1029/2021JC017938.

Martins, K., Blenkinsopp, C.E., Power, H.E., Bruder, B., Puleo, J.A., Bergsma, E.W.J., 2017. High-resolution monitoring of wave transformation in the surf zone using a LiDAR scanner array. Coast. Eng. 128, 37–43. https://doi.org/10.1016/j.coastaleng.2017.07.007.

Martins, K., Blenkinsopp, C.E., Zang, J., 2016. Monitoring individual wave characteristics in the inner surf with a 2-dimensional laser scanner (LiDAR). J. Sens. 1–11. https://doi.org/10.1155/2016/7965431, 2016.

Martins, K., Bonneton, P., Mouragues, A., Castelle, B., 2020. Non-hydrostatic, Non-linear Processes in the Surf Zone. JGR Oceans 125 e2019JC015521. https://doi.org/10.1029/2019JC015521.

Masselink, G., Castelle, B., Scott, T., Dodet, G., Suanez, S., Jackson, D., Floc'h, F., 2016. Extreme wave activity during 2013/2014 winter and morphological impacts along the Atlantic coast of Europe. Geophys. Res. Lett. 43, 2135–2143. https://doi.org/10.1002/2015GL067492.

Mosbrucker, A.R., Major, J.J., Spicer, K.R., Pitlick, J., 2017. Camera system considerations for geomorphic applications of SfM photogrammetry. Earth Surf. Process. Landforms 42, 969–986. https://doi.org/10.1002/esp.4066.

Nicholls, R.J., Townend, I.H., Bradbury, A.P., Ramsbottom, D., Day, S.A., 2013. Planning for long-term coastal change: experiences from england and wales. Ocean Eng. 71, 3–16. https://doi.org/10.1016/j.oceaneng.2013.01.025.

Nocerino, E., Menna, F., Gruen, A., Troyer, M., Capra, A., Castagnetti, C., Rossi, P., Brooks, A.J., Schmitt, R.J., Holbrook, S.J., 2020. Coral reef monitoring by scuba divers using underwater photogrammetry and geodetic surveying. Rem. Sens. 12, 3036. https://doi.org/10.3390/rs12183036.

O'Dea, A., Brodie, K., Elgar, S., 2021. Field observations of the evolution of plunging-wave shapes. Geophys. Res. Lett. 48. https://doi.org/10.1029/2021GL093664.
Ojeda, E., Guillén, J., 2008. Shoreline dynamics and beach rotation of artificial embayed beaches. Mar. Geol. 253, 51–62. https://doi.org/10.1016/j.margeo.2008.03.010.
O'Reilly, W.C., Herbers, T.H.C., Seymour, R.J., Guza, R.T., 1996. A comparison of directional buoy and fixed platform measurements of pacific swell. J. Atmos. Ocean. Technol. 13, 231–238. https://doi.org/10.1175/1520-0426(1996)013<0231:ACODBA>2.0.CO;2.
Palmsten, M.L., Brodie, K.L., 2022. The coastal imaging research Network (CIRN). Rem. Sens. 14, 453. https://doi.org/10.3390/rs14030453.
Park, H.S., Sim, J.S., Yoo, J., Lee, D.Y., 2011. Breaking wave measurement using terrestrial LIDAR: validation with field experiment on the mallipo beach. J. Coast Res. 1718–1721.
Phillips, M.S., Blenkinsopp, C.E., Splinter, K.D., Harley, M.D., Turner, I.L., 2019. Modes of berm and beachface recovery following storm reset: observations using a continuously scanning lidar. J. Geophys. Res. Earth Surf. 124, 720–736. https://doi.org/10.1029/2018JF004895.
Rattray, A., Ierodiaconou, D., Womersley, T., 2015. Wave exposure as a predictor of benthic habitat distribution on high energy temperate reefs. Front. Mar. Sci. 2. https://doi.org/10.3389/fmars.2015.00008.
Rocha, M.V.L., Michallet, H., Silva, P.A., 2017. Improving the parameterization of wave nonlinearities – the importance of wave steepness, spectral bandwidth and beach slope. Coast. Eng. 121, 77–89. https://doi.org/10.1016/j.coastaleng.2016.11.012.
Rupnik, E., Daakir, M., Pierrot Deseilligny, M., 2017. MicMac – a free, open-source solution for photogrammetry. Open Geospatial Data Softw. Stand. 2, 14. https://doi.org/10.1186/s40965-017-0027-2.
Sawada, N., Inazu, D., Wu, L., Ikeya, T., Okayasu, A., 2024. Air-borne stereo observation of ocean wave height using two independent cameras from a single unmanned aerial vehicle. J. Mar. Sci. Technol. https://doi.org/10.1007/s00773-024-01005-3.
Torkan, M., Janiszewski, M., Uotinen, L., Baghbanan, A., Rinne, M., 2022. Photogrammetric method to determine physical aperture and roughness of a rock fracture. Sensors 22, 4165. https://doi.org/10.3390/s22114165.
Van Der A, D.A., O'Donoghue, T., Ribberink, J.S., 2010. Measurements of sheet flow transport in acceleration-skewed oscillatory flow and comparison with practical formulations. Coast. Eng. 57, 331–342. https://doi.org/10.1016/j.coastaleng.2009.11.006.
Vieira, M., Guimarães, P.V., Violante-Carvalho, N., Benetazzo, A., Bergamasco, F., Pereira, H., 2020. A low-cost stereo video system for measuring directional wind waves. J. Mar. Sci. Eng. 8, 831. https://doi.org/10.3390/jmse8110831.
Vieira, M., Soares, C.G., 2024. Nearshore wind-wave spectrum estimation with a low-cost video system. In: Advances in Maritime Technology and Engineering. Taylor & Francis.